PART I

DENSIFICATION

1

SINTERING: FUNDAMENTALS AND PRACTICE

RAJENDRA K. BORDIA AND HÉCTOR CAMACHO-MONTES

1.1 INTRODUCTORY OVERVIEW

Although sintering has been practiced for thousands of years [1], significant advances in scientifically understanding the phenomenon have been made only in the last six decades. In a broad sense, sintering is the extension of the contact area between powder particles by the transport of material to or around pores under appropriate conditions of temperature, pressure, and environment [2]. The goal of the sintering practice, in general, is to produce a coherent body (from rather fragile green bodies) with controlled microstructure, in some cases with controlled porosity [3, 4]. The emphasis of sintering theory, modeling, and analysis is to predict the path of the microstructural development and its dependence on controllable parameters (e.g., temperature, time, environment, and particle size).

Numerous attempts have been made to model the sintering phenomenon, and many experimental studies have been conducted to evaluate the theories and also the important effects of process parameters. Some of the important aspects of the sintering theory and practice are reviewed in this chapter. Readers are referred to many excellent reviews, monographs, and textbooks for a more in-depth study [5–16]. Section 1.2 deals

Ceramics and Composites Processing Methods, First Edition. Edited by Narottam P. Bansal and Aldo R. Boccaccini.

with the physical description of the process, viz., the stages of sintering and the thermodynamic driving force for sintering. The next three sections deal with the classical models for sintering (Section 1.3 for viscous sintering, Section 1.4 for solid-state sintering, and Section 1.5 for liquid-phase sintering [LPS]). Section 1.6 focuses on constrained sintering and Section 1.7 summarizes the advanced kinetic and microstructural evolution models. Section 1.8 focuses on the effect of external stresses on sintering. Section 1.9 focuses on the newly discovered significant effect of external fields on sintering. Finally, in Section 1.10, some of the important aspects of sintering practice are presented.

1.2 PHYSICAL DESCRIPTION

1.2.1 The Stages of Sintering

It is widely accepted to divide the overall sintering process in three sequential stages. In general, these stages are not discrete, and usually, there is a considerable overlap between two consecutives ones. These stages are defined according to the morphology of the grains and the porosity.

The first stage or the *initial stage* of sintering corresponds to the situation when necks are forming and growing between particles, and they remain distinct as shown schematically in Figure 1.1a,b. At the end of this stage, the contact area increases by up to 20% with only a small densification (interparticle penetration). Consequently, the compact densification is only a few percent. A marked decrease in the specific surface area of the compact occurs due to surface smoothing. The grain boundaries between the particles remain in the contact plane due to the tensile stresses resulting from the surface tension.

The second stage, or the *intermediate stage* of sintering, is characterized by a more or less continuous network of pore channels along the grain edges (Fig. 1.1c). During this stage, the pore channel shrinks and grains grow. Most of the densification, and also the growth in the contact area, occurs during this stage.

The pore channels continue to shrink until they pinch off and form isolated spheriodized pores (Fig. 1.1d). This marks the beginning of the third or the *final stage* of densification. In this stage, the pore volume fraction asymptotically approaches zero. In some cases, these closed pores may trap gases, making their elimination difficult.

1.2.2 The Thermodynamic Driving Force

There is broad agreement in the literature regarding the driving force for sintering. The starting particulate configuration is far from the equilibrium state, and the driving force comes from the excess free energy. Hence, the reduction of the free energy is taken as the sintering driving force.

This excess free energy exits in the powder compact due to the large surface area and defects. In the classical sintering literature, emphasis has been on the excess free energy due to surfaces. As sintering proceeds, porosity decreases, leading to a reduction

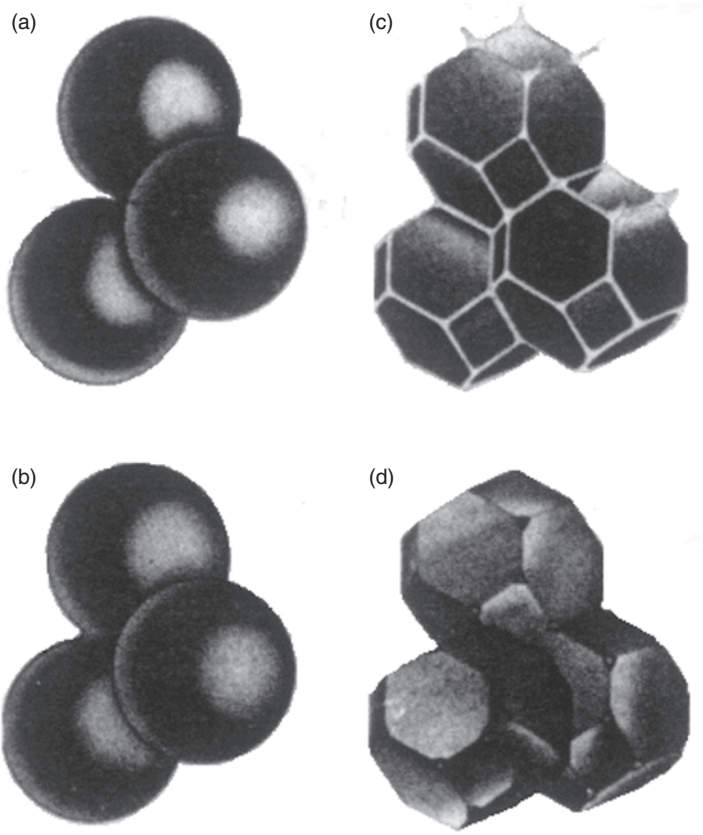

Figure 1.1. Illustrations of the stage of sintering: (a) initial stage—spheres in tangential contact; (b) near the end of the initial stage, the neck between particles starts to grow; (c) intermediate stages with continuous pore channels at grain edges and large contact area between grains; (d) final stage, tetrahedral pores at four grain intersections. Reprinted with permission from Coble [17], copyright 1961, American Institute of Physics.

of the solid–vapor interfacial area. The solid–vapor interfaces are replaced by solid–solid interfaces. When grain growth occurs, the solid–solid interfacial area also decreases. Thermodynamically, the change in free energy can be written as

$$\delta G_{\text{system}} = \delta \int \gamma_{\text{SV}} dA_{\text{SV}} + \delta \int \gamma_{\text{SS}} dA_{\text{SS}}, \tag{1.1}$$

where δG_{system} is the change in the free energy of the sintering system, γ_{SV} is the energy per unit area of the solid–vapor interface, and γ_{SS} is the energy/area of the solid–solid interface. In this equation, during sintering, the first term is negative since the area of the solid–vapor interface (A_{SV}) decreases. Considering that grain growth implies a

decrease of the solid–solid interface, the second term may be either positive or negative since grain boundary area (A_{SS}) may increase or decrease depending on how fast grain growth is going on. If grain growth does not occur, the second term is always positive as grain contacts grow during sintering. As long as δG_{system} is negative, a driving force for sintering exits.

Some powder preparation techniques like mechanical milling increase the defect concentration. In many cases, high defect concentration leads to faster sintering because of higher diffusion. Hence, the process of defect reduction may enhance the sintering driving force.

There are two distinct pathways of total energy reduction. If the surface energy (γ_{SV}) is more than the solid–solid surface energy (γ_{SS}) (true for all crystalline solids), then, in the early stages of sintering, the total energy can be lowered by the transport of atoms from the contact area to the pore, leading to a reduction in the solid–vapor interface (A_{SV}) and an increase in the grain boundary area (A_{SS}). This would lead to a reduction in the total pore volume, leading to an increase in density. This process is called *densification*. Another process is the transport of material from one part of the pore to another (e.g., in the case where the pore surface has different radii of curvature). In this case, the pore surface area decreases, but its volume does not change. In addition, there is no change in the solid–solid surface area. This process is called *coarsening*. Another example of coarsening is the coalescence of small pores in to a large pore. In this case also, the solid–vapor area decreases without any change in the pore volume.

In practice, densification and coarsening are concurrent and competing processes since they both reduce the driving force for sintering (excess surface energy). Note that coarsening is a relevant consideration only for the sintering of crystalline materials. Amorphous materials do not have grain boundaries and hence the solid–solid surface energy (γ_{SS}) is identically equal to zero. If the goal is to produce a high-density final product of crystalline materials, the coarsening processes must be suppressed. Some of the successful sintering practices do this quite effectively as discussed in Section 1.10.

1.3 VISCOUS SINTERING

For amorphous materials, sintering proceeds due to transport of matter over the entire volume, and in general, sintering proceeds at a fast rate. In addition, there is no interface between the particles (no grain boundaries). Thus, the overall energy always decreases due to the reduction of the solid–vapor interfacial area. Amorphous materials have lower viscosity (than their crystalline counterpart), and the entire solid part is involved in matter transport as schematically shown in Figure 1.2. Therefore, from a processing point of view, viscous sintering offers significant advantages. However, from a performance standpoint, viscous materials may not be desirable.

For viscous sintering, the three stages have been analyzed by Frenkel (initial stage), Scherer (intermediate stage), and Mackenzie–Shuttleworth (MS) (final stage). The kinetics of viscous sintering can be calculated following the energy balance approach

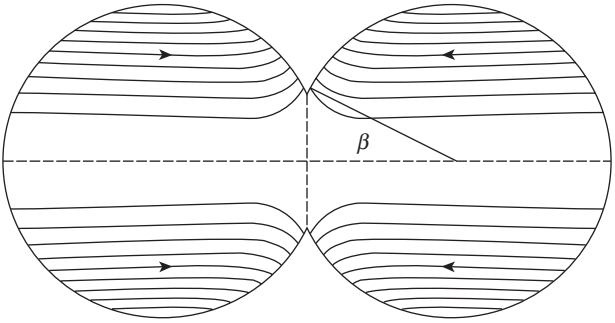

Figure 1.2. Viscous flow during amorphous sintering. Reprinted with permission from Martínez-Herrera and Derby [18], copyright 1995, John Wiley & Sons.

suggested by Frenkel [19]. In this under quasi equilibrium, the energy gained by the reduction in the surface area is dissipated in viscous flow leading to

$$\dot{E}_S + \dot{E}_f = 0, \tag{1.2}$$

where $\dot{E}_S$ and $\dot{E}_f$ are the energy rates for surface area reduction and viscous flow. This balance has also been considered by Scherer [20] and Mackenzie and Shuttleworth [21].

Frenkel analyzed the kinetics of the initial stage of viscous sintering and developed the following relationship for the sintering of spheres by viscous flow [19]:

$$\beta^2 = \frac{3\gamma t}{2\pi\eta R}, \tag{1.3}$$

where β is the angle shown in Figure 1.2.

Scherer [20] used a cell model to geometrically describe the intermediate sintering state, and Mackenzie and Shuttleworth [21] used a closed porosity model for the final stage. These two models have the capacity to describe experimental results very well. The advantage of the Scherer model is that it can describe the sintering over a very broad density range. For example, it has been successfully used to determine the densification rate of sol–gel-derived low initial density systems. The Scherer cell model works well up to a relative density of 0.95. The MS model describes the late stages including the final stages of sintering. Both models have been proposed and used to successfully calculate the sintering kinetics over a broad density range. It has been shown that in the relative density interval of 0.3–0.95, the two models predict the same densification kinetics, which has been confirmed experimentally for several systems.

The MS analysis of a spherical shell is a description of the final stage when the pores become isolated. The free sintering rate for the MS model is given by [21]

$$\dot{\varepsilon}_f = -\frac{1}{2}\left(\frac{4\pi}{3}\right)^{1/3}\left(\frac{\gamma n^{1/3}}{\eta}\right)\left(\frac{1}{\rho}-1\right)^{2/3}, \tag{1.4}$$

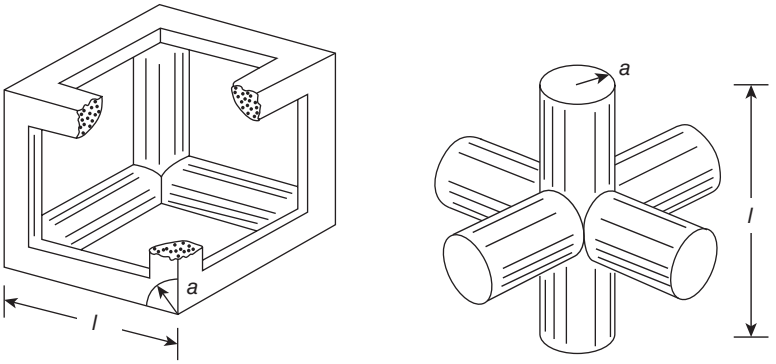

Figure 1.3. Cylindrical array geometric unit cell for the Scherer cell model. Reprinted with permission from Scherer [20], copyright 1991, John Wiley & Sons.

where n is the number of pores per unit volume, ρ is the normalized density (normalized by the theoretical density), η is the viscosity of the material, and γ is the surface energy.

For the intermediate stage of sintering, Scherer proposed the cell model shown in Figure 1.3. It was originally developed for gels and other low-density materials. In this model, an array of cylinders meet at right angles.

For this model, Scherer derived a densification rate given by [20]

$$\dot{\varepsilon}_f = -\left(\frac{\gamma n^{1/3}}{\eta}\right)\frac{\pi - 4\sqrt{2}x}{x^{1/3}\left(3\pi - 8\sqrt{2}x\right)^{2/3}}. \tag{1.5}$$

The relative density ρ and x are related through the equation

$$\rho = 3\pi x^2 - 8\sqrt{2}\,x^3. \tag{1.6}$$

Using the geometric model shown in Figure 1.3, Scherer derived the number density of pores in terms of the geometric parameters and green density [20]:

$$n^{1/3} = \frac{1}{l_0 \rho_0^{1/3}}, \tag{1.7}$$

where

$$l_0 = \frac{\sqrt{\pi}\, d_0}{2\left(1 - 2x_0\right)^2} \tag{1.8}$$

and x_0 is the root of Equation 1.6 considering that $\rho = \rho_0$, where ρ_0 is the initial relative density and d_0 is the initial particle diameter. In the density range of 0.3–0.95, both the

MS (Eq. 1.4) and the Scherer models (Eq. 1.5) give the same dependence of the densification rate on the density.

In addition, the Scherer cell model provides a method to calculate the viscous Poisson's ratio and the uniaxial viscosity as a function of the relative density (discussed in detail in Section 1.6). These equations work well over the entire densification cycle:

$$\nu_p = \frac{1}{2}\left[\frac{\rho}{3-2\rho}\right]^{1/2} \tag{1.9}$$

and

$$E_p = 3\eta\frac{\rho}{3-2\rho}. \tag{1.10}$$

The use of these parameters for sintering problems will be discussed in Section 1.6.

1.4 SOLID-STATE SINTERING

Solid-state sintering is the relevant mechanism for crystalline materials. Even though it has common features with viscous sintering for amorphous powder compacts, the physical picture has remarkable differences. The first difference is that not the entire solid body is involved in sintering. The transport of matter is highly localized and occurs in the vicinity of the pores. This leads to several mechanisms depending on the source, sink, and the matter transport path. For initial-stage sintering, the solid-state sintering mechanisms are shown in Figure 1.4 and are described in Table 1.1.

For solid-state sintering, the matter sources and sinks are surfaces, grain boundaries, and line defects; this is a characteristic and defining feature of the sintering of crystalline. For amorphous materials, the entire solid is involved in matter transport. In contrast, in solid-state sintering, defects (including surfaces and boundaries) are the focal points for matter transport.

For the solid-state sintering, we can hypothetically consider two reference volumes as shown in Figure 1.4. Volume V1 is in the equilibrium part of the particles and volume V2 includes defects (such as grain boundaries or surfaces). The free energy for volume V2 is higher than that of volume V1. This free energy difference is the driving force for material transport leading to solid-state sintering.

1.4.1 Initial-Stage Solid-State Sintering Models

Following Frenkel [19] and Kuczynski's [23] pioneering work, numerous models for initial-stage solid-state sintering have been developed. These models predict the rate of neck growth and densification for simple geometries like a pair of wires or spheres. Equations have been proposed to calculate the neck size as a function of time for different transport mechanisms, for example, Equation 1.11. Ashby developed an elegant, graphical approach to capture the regions of dominance of different mechanisms in

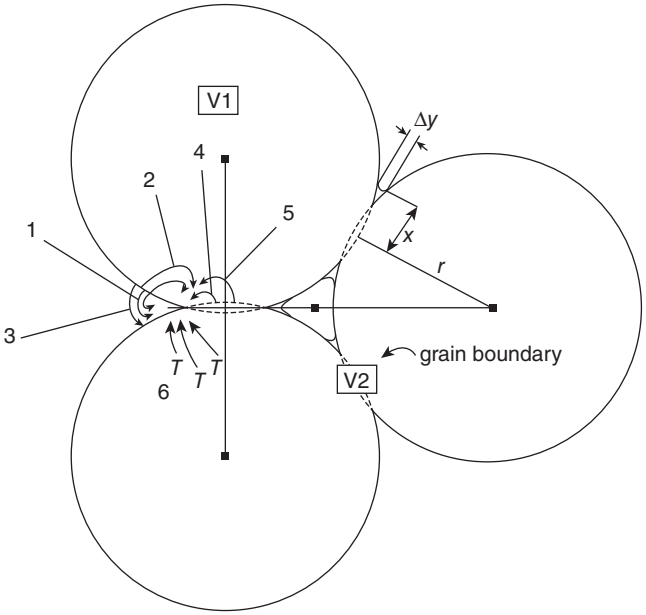

Figure 1.4. Six paths for matter transport. All lead to neck growth. Only mechanisms 4, 5, and 6 lead to densification (see Table 1.1 for sources and sinks for each path). Reprinted with permission from Kingery et al. [22], copyright 1975, John Wiley & Sons.

TABLE 1.1. The Transport Paths, Sources, and Sinks of Matter and Whether Densification Occurs or Not for Various Initial-Stage Sintering Mechanisms

Mechanism No.	Tranport Path	Source of Atoms	Sink of Atoms	Densification
1	Surface diffusion	Surface	Neck	No
2	Lattice diffusion	Surface	Neck	No
3	Vapor transport	Surface	Neck	No
4	Boundary diffusion	Boundary	Neck	Yes
5	Lattice diffusion	Boundary	Neck	Yes
6	Lattice diffusion	Dislocations	Neck	Yes

For a schematic illustration of the mechanism, see Figure 1.4 [22].

"sintering maps" [24]. Although all transport mechanisms contribute to neck growth, the rates for each mechanism are different and Ashby's sintering maps [24, 25] provide a convenient graphical visualization of the dominant mechanisms for a given set of temperature, neck size, and particle size. In these sintering maps, at the boundaries between two fields, the neck growth rates from the two neighboring mechanisms are the same. Far away from the boundaries, a particular mechanism dominates. Figure 1.5 shows an example of a sintering map for copper spheres with radii of 57 μm.

One of the most important applications of this approach analysis has been in identifying the dominant mechanism for sintering under a given set conditions. The experi-

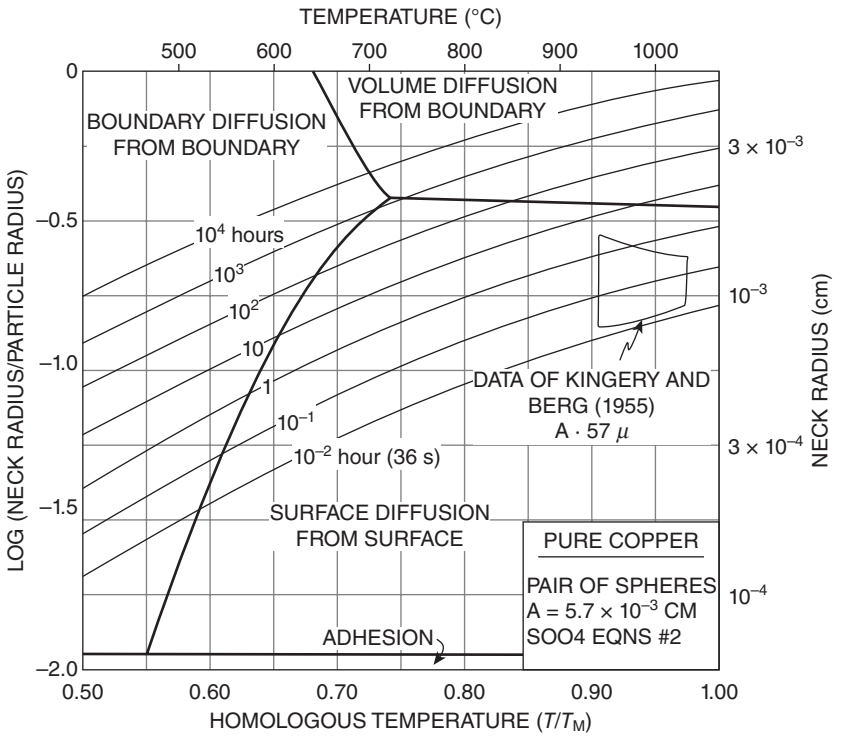

Figure 1.5. Sintering map for copper powder. Reprinted with permission from Ashby [24], copyright 1974, Elsevier.

ments are conducted on model systems like two spheres, or two wires, or a sphere and a plate. The neck size is measured as a function of time. Several authors, including Kuczynski, have supported the relation

$$\left(x^n / a^m\right) \alpha\, t, \tag{1.11}$$

where x and a are half the neck radius and the particle radius, respectively, and t is the sintering time (typically, time at a specific isothermal sintering temperature).

The values of the exponents n and m for different mechanisms and calculated by different investigators are given in Table 1.2. Also included in the table are the values of the scaling exponent, z, as proposed by Herring [26]. According to this, if two partially sintered systems are geometrically similar, except that the linear dimension of one system is λ times the other, then the time required to produce geometrically similar changes in the two systems, at the same temperature, is very simply related as

$$\Delta t_2 = \lambda^z \Delta t_1. \tag{1.12}$$

z depends on the mechanism of sintering (Table 1.2).

TABLE 1.2. Values of Exponents *n*, *m*, and *z* in Equations 1.11 and 1.12 Calculated by Different Authors for Initial-Stage Sintering Mechanisms

Mechanism	Author	*n*	*m*	*z*
1	Kuczynski [23]	7	3	4
	Burton et al. [27]	5	2	
	Pines et al. [28]	6	2	
	Rockland [29]	7	3	
2	Kuczynski [23]	5	2	3
	Cabrera [27]	5	2	
	Pines et al. [28]	4	1	
	Rockland [30]	5	2	
3	Kuczynski [23]	3	2	2
	Kingery and Berg [31]	3	1	
	Pines et al. [28]	7	3	
	Hobbs and Mason [32]	5	2	
4	Rockland [30]	6	2	–
	Coble [33]	6	2	
	Johnson [34]	6	2	
5	Rockland [30]	4	1	–
Viscous	Frenkel [19]	2	1	1

The mechanism numbers correspond to those in Table 1.1.

Many experimental studies have been conducted to test these models (Eqs. 1.11 and 1.12). However, the approach has come under considerable criticism regarding, for instance, the simplifying assumptions for the neck geometry and the inability, experimentally, to ensure that a single mechanism dominates. This has resulted in an inability to critically evaluate the predictions of the models. In spite of this criticism, this approach has led to important technological implications including strategies to suppress the coarsening mechanism and the significant importance of fine particle size. For example, Herring's scaling law suggests that decreasing the particle size by an order of magnitude would lead to a reduction in the sintering time of 10–10^4. As will be highlighted in Section 1.10, this realization has led to significant attention on making and processing ultrafine and nanoscale powders.

1.4.2 Intermediate-Stage Solid-State Sintering Models

A representative model for the solid-state sintering intermediate stage has been proposed by Coble [17]. Microstructure with porosity is modeled as cylinders around the edges of tetrakaidecahedron-shaped grains (Fig. 1.6). The densification rate is calculated for the case of matter transport by volume and grain boundary diffusions. For volume diffusion, the densification rate is given by

$$\frac{1}{V}\frac{dV}{dt} = -457\frac{D_V \gamma \Omega}{kTd^3}, \tag{1.13}$$

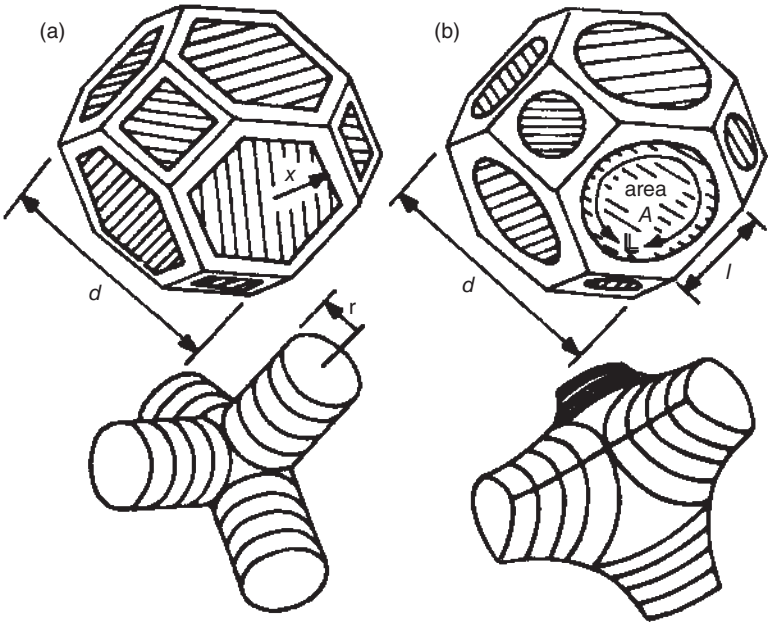

Figure 1.6. Representative unit cell for intermediate-stage solid-state sintering. (a) Original model of Coble [17] and (b) modification by Beere [38].

and for grain boundary diffusion, the densification rate is given by

$$\frac{1}{V}\frac{dV}{dt} = -40\frac{\delta_b D_b \gamma \Omega}{kTd^4}\frac{l}{r}, \tag{1.14}$$

where $1/V\ dV/dt$ is the volumetric densification rate. D_v and D_b are the diffusion coefficients for volume and grain boundary diffusion, respectively. Ω is the atomic volume, γ is the surface energy, δ_b is the width for grain boundary diffusion, k is the Boltzmann constant, and T is the absolute sintering temperature. The parameters r, l, and d characterize the microstructure, and they are shown in Figure 1.6.

Johnson [35] and Eadie et al. [36, 37] have used similar geometry but allowed for parallel transport paths. Johnson [35] has developed the shrinkage rate for combined volume and grain boundary diffusions in terms of geometric parameters and has obtained the following densification rate:

$$\frac{1}{V}\frac{dV}{dt} = -8\frac{\bar{H}\gamma\Omega}{\bar{x}kT}\{D S_V + \delta_b D_b L_V\}, \tag{1.15}$$

where $\bar{H}$ and $\bar{x}$ are the average value of the pore curvature and of the grain boundary radius, respectively. S_V is the pore surface area per unit volume and L_V is the length of the grain boundary/pore intersection per unit volume.

Apart from this, the only other significant development to intermediate-stage sintering has been the work of Beere [38]. In this work, the pore is assumed to have a thermodynamically correct shape requiring the correct dihedral angle (Fig. 1.6b). The pore shape is calculated by minimizing the surface area for a fixed volume. The calculated densification then depends on the dihedral angle (θ). The calculated densification rate shows that fast densification is possible for materials with large dihedral angles. Small values of the dihedral angle have been given as one of the reasons for difficulty in sintering covalent solids. The pore shapes assumed by Beere have been experimentally confirmed by Lee et al. [39]. The rate expressions given by these various intermediate-stage models have been reviewed by Beere [40]. It has been shown that densification rates predicted by various models can differ by as much as two orders of magnitude, and Coble's relation gives the lowest rates.

An important criticism of these models has been the fact that none of them take care of concurrent grain growth. In addition, the geometric model of uniform pores and grain throughout the sintering body is far from correct [41]. Coble [17] introduced an empirical grain growth equation. This equation assumes the volume of individual grains to be proportional to sintering time. With this assumption, the well-known semilogarithmic sintering law was derived:

$$P - P_0 = K \ln\left(\frac{t}{t_0}\right), \tag{1.16}$$

where K contains all material parameters for sintering and grain growth. P_0 and t_0 are the porosity and the time at the onset of intermediate-stage sintering. In spite of the criticism regarding idealized geometry, Coble's equation has been extensively used to analyze experimental results. It has been shown to semiquantitatively predict experimental results for a wide variety of materials.

1.4.3 Final-Stage Solid-State Sintering Models

This stage of sintering is geometrically the simplest. The pore is isolated and assumed to be at four grain junctions. Coble [17] has calculated the rate of densification for this geometry. Additional models are those derived from creep cavitation literature [42–44]. The porosity is modeled as equilibrium-shaped cavities on the grain boundaries, and the densification rate is calculated by deriving the rate of shrinkage of these cavities under the compressive surface tension force. The practical difficulties that arise in this stage of densification are

i. abnormal grain growth, which leaves pores inside the grains, and
ii. slowly diffusing entrapped gases in the closed pores. This essentially leads to termination of shrinkage when the gas pressure within the pores equals the surface pressure. In addition, the trapped gas can change the equilibrium dihedral angle and can further affect shrinkage.

One of the most serious shortcomings of the intermediate- and final-stage sintering models has been that the calculated diffusion coefficients and the activation energy

from sintering are higher than those obtained from tracer diffusion experiments. Various explanations have been provided for this discrepancy, but none of them have been satisfactory.

1.4.4 Pore–Boundary Interaction

During the intermediate and final stages of sintering of crystalline materials, there is a strong interaction between grain boundaries and pores. Alexander and Balluffi, in their classical experiments on copper wires, showed that only the pores that were on the grain boundaries shrank [45]. As a result, normal grain growth has been investigated in detail in porous materials. It was shown that pores on the boundary lead to a reduction in grain growth rate [46, 47]. A very significant advance in the understanding of grain growth in porous materials was made initially by Kingery and Francois [48] and later extended by Brook [49]. As curved boundaries move during grain growth, the pores can either remain attached to the boundary or be left behind. In the case in which they remain attached, the velocity of the boundary could be limited by pore mobility (boundary mobility higher than pore mobility) or by the intrinsic mobility of the boundary (pore mobility higher than boundary mobility). By using standard expressions for pore and boundary mobility, regimes of grain size and pore size were identified in which separation occurs. It was shown that in the intermediate pore size, separation occurs. Very small pores remain attached to the boundary whose velocity is controlled by intrinsic boundary mobility. Large pores also remain attached to the boundary, but in this case, the pores control the boundary mobility.

This analysis was further refined by Hsueh et al. [50, 51]. They properly calculated the pore and boundary mobility in porous materials and showed the important effect of dihedral angle. The pore velocity was shown to be a function of dihedral angle, and it was shown that the pore size should be below a critical size (which depends on the grain size and dihedral angle) to avoid pore breakaway.

Another important effect of dihedral angle and pore–boundary interaction was highlighted by Kellett and Lange [52]. It was shown that thermodynamically, some pores grow and others shrink. The condition of pore stability is governed by the dihedral angle and the number of nearest neighbors. It was shown that materials with low dihedral angles are difficult to sinter to high density, and this is one of the reasons for the difficulty in sintering covalent materials that have low dihedral angles.

1.5 LPS

The differences between viscous and solid-state sintering have been pointed out in the previous sections. Practically, it would be desirable to develop a fast sintering approach for solid-state materials. In some ways, this is possible through the technique known as LPS. In addition, for covalent materials, due to their low dihedral angles, solid-state sintering is almost impossible. In these cases also, LPS is the preferred sintering approach. In LPS, the system has a small volume fraction of viscous liquid phase at the sintering soak temperature. This fraction is generally less than 5 vol %. It is

customary to use a practical nomenclature for these compounds. The particle solid forming the major component is written first, and the liquid producing component is written in parentheses, for example, Si_3N_4(MgO) and ZnO(Bi_2O_3), where MgO and Bi_2O_3 are the additives that lead to the formation of the liquid phases for Si_3N_4 and ZnO, respectively.

What LPS has in common with other sintering techniques is that the process is divided in three stages and that the driving force is connected with the decreases of free energy and surface area. However, the mechanisms and the structural evolution are quite different from other techniques. First, it is necessary to emphasize that a necessary condition for LPS is that the liquid must wet the solid phase. Figure 1.7 illustrates the wetting behavior between a liquid and a solid, schematically showing cases of nonwetting and wetting liquids.

Good or complete wetting is a precondition for LPS. Ideally, the liquid phase should perfectly wet the grain surfaces as shown in Figure 1.8 [54]. Then, the matter

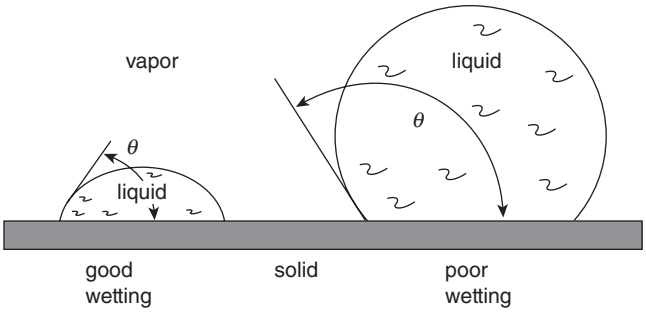

Figure 1.7. Wetting behavior between a liquid and a solid showing good wetting and poor wetting. The wetting angle θ is governed by the thermodynamic equilibrium between the different surface energies. Reprinted with permission from German et al. [53], copyright 2008, Springer.

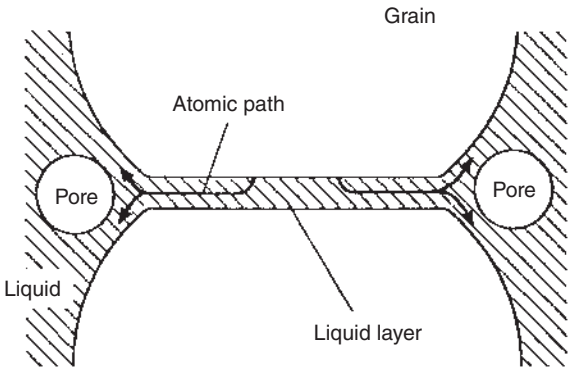

Figure 1.8. Schematic of an idealized liquid-phase sintering microstructure. Reprinted with permission (via Copyright Clearance Center) from Rahaman [54], copyright 1995, CRC Press.

transport occurs through the liquid, leading to an enhancement of the densification rate due to the higher diffusion or lower viscosity of the liquid phase. Ideally, pores should be trapped in the liquid phase (as opposed to being at the liquid–solid surface). The pressure difference across the surface of a spherical pore of radius r in the liquid phase may be described by the equation

$$\Delta p = -\frac{2\gamma_{lv}}{r}, \tag{1.17}$$

where γ_{lv} is the liquid–vapor surface energy.

This pressure difference is the driving force for LPS. Kinetically, LPS is also divided in three stages. They are (1) rearrangement, (2) solution–precipitation, and (3) Ostwald ripening. These stages are schematically illustrated in Figure 1.9.

Rearrangement takes place as the liquid phase is formed. For a successful LPS, the composition of the powder compact must be such that good wetting between the liquid and the solid particle is achieved. In addition, it is also important to have low liquid solubility in the solid and higher solid solubility in the liquid. At this point, the tendency for the system to decrease the surface energy results in capillary forces

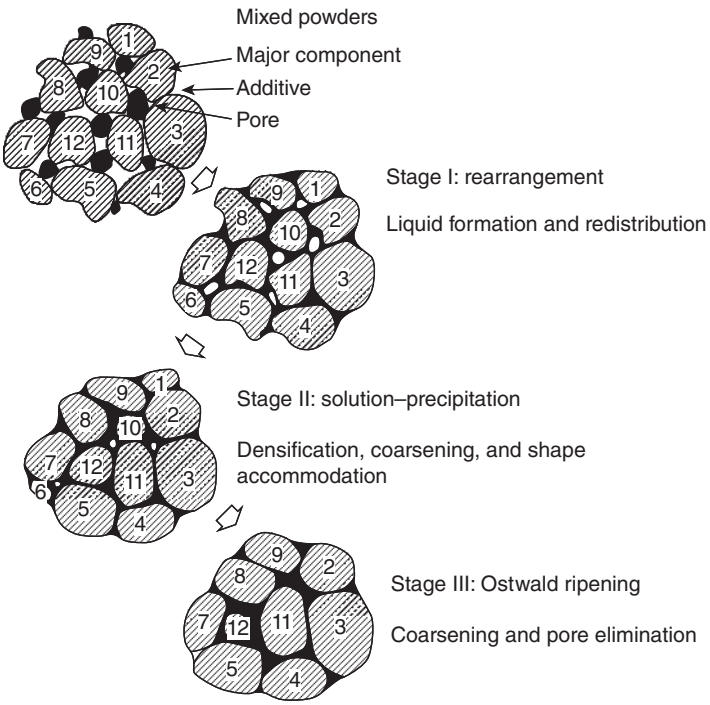

Figure 1.9. Stages of liquid-phase sintering. Reprinted with permission (via Copyright Clearance Center) from Rahaman [54], copyright 1995, CRC Press.

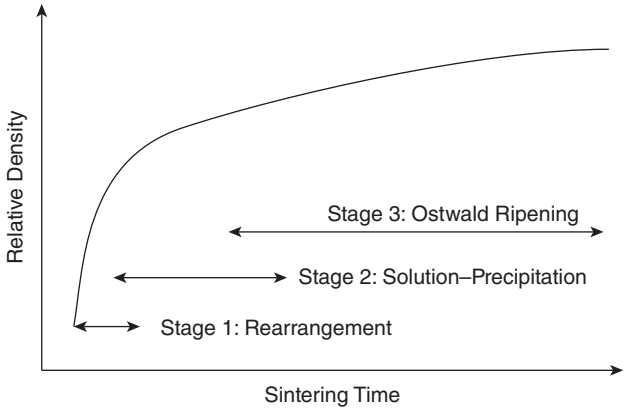

Figure 1.10. Schematic diagram illustrating the three stages of liquid-phase sintering curves. Reprinted with permission (via Copyright Clearance Center) from Rahaman [54], copyright 1995, CRC Press.

that play a key role in the particle rearrangement. Shrinkage and densification may occur as can be observed in Figure 1.10. In general, the first stage only lasts a few minutes.

As densification by rearrangement slows, the solution precipitation process becomes dominant. Solution of the solid phase takes place at the interfaces with higher chemical potential; matter is transported through the liquid phase and precipitated at a liquid–solid interface with lower chemical potential. Then, as shown in Figure 1.8, a bridge is formed between contact particles and the capillary force may attract a particle. During this stage, densification is accompanied by considerable coarsening (grain growth) and by grain shape changes.

When the Ostwald ripening process becomes dominant, that is, grain coarsening due to the solution–precipitation process, the third stage of the LPS has started. This is the longest-lasting stage where densification is slow (Fig. 1.10). During this stage, grain shape accommodation allows a more efficient packing of the structure as shown in Figure 1.11. The degree of change in the grain morphology and accommodation depends on the fraction of the liquid phase. For a higher liquid volume fraction, more shape change and accommodation takes place.

Polycrystalline particles go through an extra process of particle rearrangement also known as secondary rearrangement [55]. Figure 1.12 illustrates this process, in which tension at the interfaces between crystallites and the liquid phase can induce the separation of crystallites such that they become individual particles.

The significant advantage of LPS is the densification enhancement and the ability to sinter materials that just cannot be sintered in the solid state (e.g., silicon nitride). As a result, this process is commonly used in sintering practice. However, the liquid phase remains as glass (amorphous phase), and this represents a problem for those applications where good mechanical properties, especially at high temperatures, are

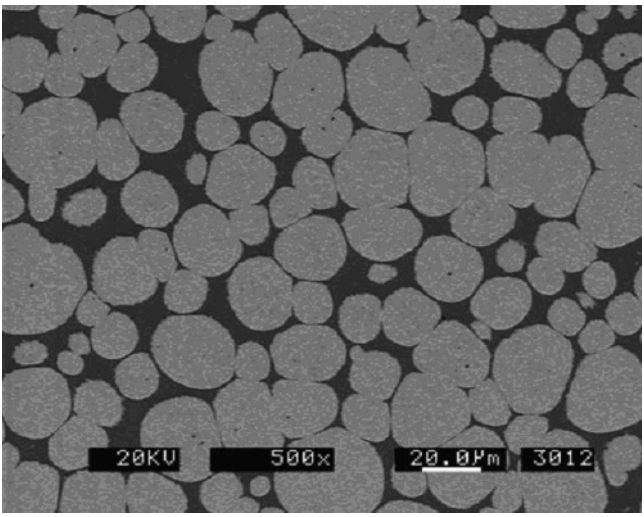

Figure 1.11. Micrographs of an 88 wt % W heavy alloy with 15.4 wt % Ni and 6.6 wt % Fe. The alloy was held for 30 min at 1500°C. Reprinted with permission from German et al. [53], copyright 2008, Springer.

Figure 1.12. Schematic of secondary rearrangement for polycrystalline particles during liquid-phase sintering.

needed. Also, the glass phase may be a disadvantage for electric and magnetic materials. Innovative strategies have been developed to minimize the glass phase including postsintering annealing steps to crystallize it.

1.6 DENSIFICATION AND DEFORMATION IN CONSTRAINED SINTERING

In many practical situations, sintering bodies are subjected to physical constraint. Specific examples include the sintering of coatings or films on dense substrates and the sintering of composites. Continuum mechanics has been used to characterize

densification and deformation during constrained sintering [56–58]. The most common approach has been to use the viscoelastic analogy. In this approach, the constitutive laws for linear viscous incompressible fluid can be written as

$$s_{ij} = 2\eta\ \dot{e}_{ij} \tag{1.18}$$

and

$$\dot{\varepsilon} = 3\dot{\varepsilon}_f. \tag{1.19}$$

Viscoelastic analogy allows us to replace the strains and the elastic coefficients in the elastic equations by corresponding strain rates and effective viscous coefficients for a porous sintering powder compact. Therefore, Equations 1.18 and 1.19 may be written as

$$s_{ij} = 2G_p\dot{e}_{ij} \tag{1.20}$$

and

$$\sigma = K_p(\dot{\varepsilon} - 3\dot{\varepsilon}_f). \tag{1.21}$$

In these relations, G_p and K_p are the shear and the bulk viscosities; s_{ij} and $\dot{e}_{ij}$ are the deviatoric stress and strain rates; σ and $\dot{\varepsilon}$ are the hydrostatic stress and the volumetric strain rates; respectively; and $\dot{\varepsilon}_f$ is the free linear strain rate (densification rate one would get in the absence of internal or external stresses) of the sintering body. Equations 1.20 and 1.21 reduce to Equations 1.18 and 1.19 for the case of fully dense (relative density equal to 1) incompressible viscous materials for which $G_p = 2\eta$ and $K_p \to \infty$. For a porous body, G_p and K_p depend on the microstructure of the sintering body and evolve as the material sinters (so does the free sintering strain rate). These parameters are called shear and bulk viscosities.

These equations are valid for linear isotropic viscous materials. It has been shown that there are many amorphous and crystalline powder compacts whose densification and deformation behavior are governed by these relations. Both viscous sintering materials (e.g., glass or filled glasses) and even polycrystalline ceramics at low stresses follow these constitutive laws. This is especially true for polycrystalline bodies if the boundaries act as a perfect source and sink for defects.

Equation 1.21 shows that the volumetric strain rate $\dot{\varepsilon}$ is a lineal superposition of the free sintering rate and the volumetric strain rate induced by the stress, where σ is the hydrostatic stress induced due to the constraint or due to external stresses.

In analogy with linear elasticity, there are two other viscous parameters for a sintering body. These are the uniaxial viscosity, E_p, and the viscous Poisson's ratio, ν_p. Analogous to linear elasticity, there are two relations between the four constitutive parameters:

$$G_p = E_p/[2(1+\nu_p)] \tag{1.22}$$

and

$$K_p = E_p /[3(1-2\nu_p)]. \tag{1.23}$$

Using the uniaxial viscosity and the viscous Poisson's ratio, Equations 1.20 and 1.21 can be rewritten as [56]

$$\dot{\varepsilon}_x = \dot{\varepsilon}_f + E_p^{-1}[\sigma_x - \upsilon_p(\sigma_y + \sigma_z)], \tag{1.24}$$

$$\dot{\varepsilon}_x = \dot{\varepsilon}_f + E_p^{-1}[\sigma_x - \upsilon_p(\sigma_y + \sigma_z)], \tag{1.25}$$

and

$$\dot{\varepsilon}_x = \dot{\varepsilon}_f + E_p^{-1}[\sigma_x - \upsilon_p(\sigma_y + \sigma_z)]. \tag{1.26}$$

These equations have been widely used to study densification and deformation during constrained sintering for isotropic powder compacts.

Using these relations, the volumetric densification rate is

$$\dot{\varepsilon}_\rho = \frac{\dot{\rho}}{\rho} = -(\dot{\varepsilon}_x + \dot{\varepsilon}_y + \dot{\varepsilon}_z). \tag{1.27}$$

As a side note, it is important to point out that the densification rates given by Equations 1.13–1.15 and 1.27 assume that the mass remains constant during sintering.

The viscous responses to uniaxial stress (E_p), to shear stress (G_p), and to hydrostatic stress (K_p) are functions of the powder compact's microstructure and density. A number of models have been proposed in the literature. Sintering microstructures are rather complex and include parameters including the relative density, average grain size, average pore size, grain size distribution, and pore size distribution. At the minimum, the models must be dependent on the density and should meet the limiting condition of incompressibility for the fully dense state. This corresponds to the viscous Poisson's ratio equal to 0.5 (equivalent to the bulk modulus, $K_p \to \infty$). One example of the microstructure-based model was presented in Section 1.3 for viscous materials. The free densification rate, $\dot{\varepsilon}_f$, the uniaxial viscosity, E_p, and the viscous Poisson's ratio, ν_p, is given by Equation 1.4 or 1.5, 1.9, and 1.10, respectively.

A significant advantage of this continuum approach is that complex sintering problems like the codensification of multimaterial systems can be analyzed. In addition, the approach can be readily implemented in numerical simulations. An example is shown in Figure 1.13 for the cofiring of a metal ceramic multimaterial system. The regions A1, A2, and A3 correspond to metal powders, and the rest of the material is a ceramic. Practically, this case is an idealized representation of surface and buried conductor lines in a dielectric in an electronic package. Figure 1.13 shows the evolution profiles for shape deformation, von Mises stresses, relative density map, and displacement field during sintering. Several important effects of constraint are highlighted in this analysis, including the "unexpected deformation" (difference from the initial shape) due to a nonuniform displacement field. The nonuniform densification is a result of the nonuniform stress distribution. In this analysis, the metal powder located in areas 1, 2, and 3

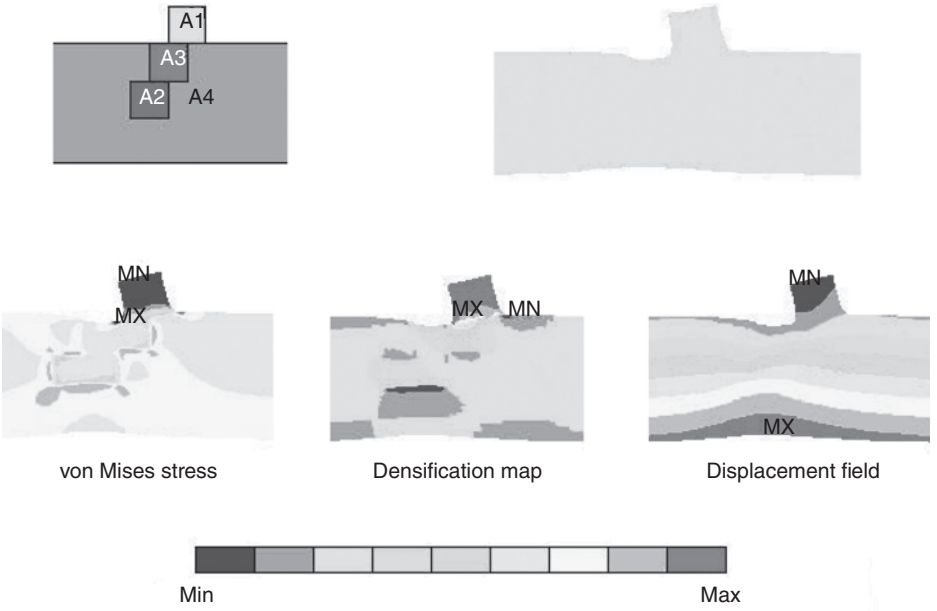

Figure 1.13. An example of the use of continuum models to numerically simulate the processing of a complex multimaterial system. Regions A1, A2, and A3 correspond to a metal powder and A4 to a ceramic powder compact.

and the ceramic powder located in area 4 are assumed to have different uniaxial viscosities and free sintering rates. Hence, these parts of the sample shrink at different rates; consequently, stress gradients appear near the interfaces between the two constituents.

In the literature, many examples of constrained sintering may be found where Equations 1.24–1.26 are used to study systems such as sintering in the presence of rigid inclusions and constrained sintering of thin films among others. Both theoretical and experimental studies have been conducted. Illustrative examples are in References 59 and 60 for sintering of composites and in References 61–63 for sintering of constrained films. It has been shown that the presence of rigid inclusions retards the densification of the matrix and under some conditions can lead to the formation of cracklike processing defects. Similarly, the densification rate of constrained films is less than that of free films, and if the films are thicker than a critical thickness, cracks perpendicular to the substrate can be formed during sintering.

1.7 MICROSTRUCTURE-BASED MODELS

1.7.1 Relationship between Mass Transport and Viscosity

Solid-state sintering is controlled by matter transport. Matter transport is driven by the chemical potential gradient. Although globally sintering is controlled by a decrease in

overall free energy (Section 1.2), the local mass transport is the mechanism of achieving this. Thus, there has to be a relation between the change in free energy and the chemical potential gradients. The gradient of chemical potential is related to material flow through the Einstein–Nernst equation:

$$J_i = \frac{\Omega \upsilon_i}{kT} D_i \cdot \nabla \mu, \tag{1.28}$$

where J_i is the mass flux, ∇ is the bidimensional gradient at the coordinate interface; υ_i is the atomic frequency, D_i is the diffusion coefficient, k is the Boltzmann constant, Ω is the atomic volume, and T is the absolute temperature.

The chemical potential at the surface ($\mu = \mu_s$) is given in terms of the surface geometry (curvature) and surface energy through the well-known Herring equation:

$$\mu_s = \mu_0 + \left[\left(\frac{1}{R_u} + \frac{1}{R_v} \right) \gamma + \left(\frac{1}{R_u} \right) \gamma n_u n_u + \left(\frac{1}{R_v} \right) \gamma n_v n_v \right] \Omega, \tag{1.29}$$

where μ_0 corresponds to the chemical potential at a plane flat surface, u and v are the local principal directions, R_u and R_v are the radii of curvature in the directions u and v, and n_u and n_v denote the second derivate of the surface energy γ with respect to the angle of the two principle directions u and v. For the case of a plane grain boundary, Herring stated that

$$\mu_s = \mu_0 - \Omega \sigma_n, \tag{1.30}$$

where σ_n is the normal component of stress at the grain boundary. In Equations 1.29 and 1.30, the surface energy and the atomic volume are material properties, then the surface curvature and boundary stress may be seen as solid-state sintering driving forces.

The combination of Equations 1.28 and 1.29 for the case of surface diffusion leads to the following relation:

$$j_i = -\frac{2\gamma_s \Omega \delta D_s}{kT} \nabla \kappa, \tag{1.31}$$

where it is assumed that $v_i = \delta/\Omega$, δ is the diffusion width, and $\nabla \kappa$ is the gradient of surface curvature (the term in the square brackets in Eq. 1.29). Combining Equations 1.28 and 1.30 for boundary diffusion leads to

$$j_i = \frac{\Omega \delta D_b}{kT} \nabla \sigma_n. \tag{1.32}$$

Equations 1.31 and 1.32 illustrate that the surface curvature gradient and stress gradient are the driving force for pore surface and grain boundary diffusion during solid-state sintering.

The energy balance can be stated as it was done for the amorphous sintering by Frenkel [19]. The rate of energy dissipation can be written as

$$\dot{W} = \frac{1}{2}\sum_{l}\left(\dot{u}_n^{(l)}F_n^{(l)} + \dot{u}_{t,i}^{(l)}F_{t,i}^{(l)}\right) = V\sigma_{ij}\dot{\varepsilon}_{ij}, \tag{1.33}$$

where ½ is to consider that each grain boundary interface belongs to two grains; the index l is for each grain boundary. V is the volume of the representative volume. $\dot{u}_n^{(l)}$ and $\dot{u}_{t,i}^{(l)}$ are the normal and the tangential components of the displacement rate of the (l)–grain contact; $F_n^{(l)}$ and $F_{t,i}^{(l)}$ are the normal and the tangential components of the force at the (l)–grain contact.

In addition, using the continuum approach, the stress and strain rates for a sintering body are related by

$$\sigma_{ij} = C_{ijkl}\dot{\varepsilon}_{kl} + \delta_{ij}\sigma_s, \tag{1.34}$$

where C_{ijkl} is the viscous coefficient; σ_s is known in the literature as the sintering stress or the sintering potential. It is defined as the external hydrostatic stress required to completely suppress sintering. Further mathematical details may be found in the literature [64–66]. The continuum relations, Equations 1.24–1.26, are related to Equation 1.34. Specifically, for an isotropic body, the sintering potential, $\sigma_s = -3K_p\dot{\varepsilon}_f$ and C_{ijkl} are general viscous coefficients, which, for an isotropic material, are given by two of the four constitutive parameters: E_p, ν_p, G_p, and K_p.

For statistically homogeneous orientation of the contacts, the material is isotropic. Then, their viscous properties may be characterized only by two constants, let say, the shear and bulk viscosities. In terms of the diffusion and material parameters, these are given by [65]

$$G_p = C_{1212} = \rho_0^{2/3}\rho^{1/3}Z\frac{3c^2}{20R}\left\{\frac{kTc^4}{12\Omega\delta D_b} + \eta_s\right\} \tag{1.35}$$

and

$$K_p = \frac{1}{3}\left(C_{1111} + C_{1122} + C_{1133}\right) = \frac{\rho_0^{2/3}\rho^{1/3}ZkTc^4}{48\Omega\delta D_b R}, \tag{1.36}$$

where ρ_0, Z, c, R, and η_s are the initial relative density, the average number of contacts per particle, the grain size, the particle size, and the sliding viscosity between particles, respectively.

Equations 1.35 and 1.36 are for connected porosity (intermediate-stage sintering); for closed porosity (final-stage sintering), the bulk viscosity is given by [65]

$$K_p = \frac{kTR^3}{18\Omega\delta D_b\rho}\left(-2\ln\omega - \frac{33}{64} + \omega - \frac{\omega^2}{16}\right). \tag{1.37}$$

ω is the area fraction of the particle contact covered by pore [65]. In order to calculate G_p, the ratio of G_p/K_p is used, which is reported to be between 0.269 and 1.5 [65]. Most models predict a gradual decrease of G_p/K_p toward zero as $\rho = 1$. This is to be expected since the bulk viscosity for a fully dense body must be infinite.

Equations 1.35–1.37 give the viscosities of a body undergoing solid-state sintering in terms of important microstructural parameters like the relative density, the number of contacts, initial density, and particle size. As can be expected, many of these parameters evolve during sintering, and therefore the constitutive parameters evolve.

Thus, it can be seen that even for isotropic sintering, the precise and correct physical description is complicated. Any simplifying assumptions must be considered carefully since their applicability may be limited. In part due to the complexity associated with the analytical description of sintering, recently, there has been a significant interest in developing a multiscale computer simulation of the process. The essential elements of this are presented next.

1.7.2 Advanced Structural Evolution Models

In the last 15 years, sintering modeling has experienced considerable advances in three main directions: (1) simulations of multiparticle systems; (2) more realistic structures as representative volumes of sintering for the analysis of complex geometries, including anisotropy; and (3) simulations at multiple-length scales. This topic is quite broad and is still developing. Here we present just a few examples of this rapidly evolving field.

1.7.2.1 Discrete Element Simulations (DESs). DES is a tool that has been recently introduced to study the microstructural evolution during the sintering of powder compacts [67, 68]. Figure 1.14 illustrates the changes in microstructure over a broad density range of a multiparticle assembly. DES provides a practical way to consider particle rearrangement because the force equilibrium is calculated for each individual particle or discrete element. Comparisons with experimental data have shown good agreement regarding the evolution of average grain size and average contact area between particles. In addition, good agreement has been shown for shrinkage and densification (between experimental results and DES simulations). Finally, DES has been also useful in describing the evolution of anisotropic microstructures and the development of defects during sintering [69, 70].

1.7.2.2 Representative Volume Elements. The representative volume first proposed by Svoboda et al. [64] and Riedel et al. [65] has been developed further to take into consideration a more realistic structural evolution [71]. Figure 1.15 shows an example with different contacts sizes. In addition, special care is focused on precise surface curvature and its evolution.

1.7.2.3 Multiscale Models. A significant advance in the simulation and understanding of the sintering phenomenon has been accomplished with the recent development of multiscale models for sintering. This is due to the realization that sintering is fundamentally characterized by phenomena at different length scales [72].

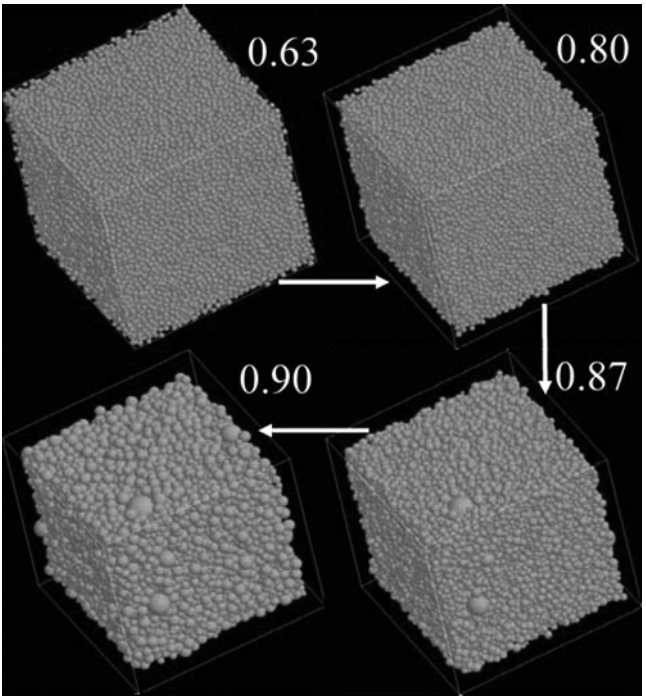

Figure 1.14. Discrete element simulations of a multiparticle system highlighting the evolution of the microstructure over a broad density range. Reprinted with permission from Martin et al. [67], copyright 2006, Elsevier.

Figure 1.16 shows the three main scales to study sintering. The macroscale is characterized by the continuum description parameters such as densification, shrinkage, strain rate, and viscosity (Section 1.6). These macroscopic parameters are a consequence of the mesostructural evolution. In the sintering literature, the mesoscale is known as the microstructural scale. Since these two scales must be connected, one must be able to obtain the parameters for the continuum scale from the mesoscale. In the literature, few studies have explicitly demonstrated this multiscale connection. For example, the Monte Carlo approach has been used to study the mesostructure evolution and coupled to the continuum description [73]. In principle, several models to estimate viscosity and free sintering rate, such as the Scherer cell model and the Riedel model, deal with the multiscale nature of sintering because their representative volume may be considered as the mesoscale models. Similarly, DES (described in Section 1.7.2.1) is an example of mesoscale simulation. Using this to obtain the parameters for the continuum scale is an example of multiscale simulations. The smallest length scale is the microscale, where simulations at the atomic scale (e.g., molecular dynamics) are used to calculate parameters like the diffusion coefficient. Olevsky has also developed an anisotropic multiscale model. He reports unexpected deformations resulting from the anisotropic nature of the porosity [74].

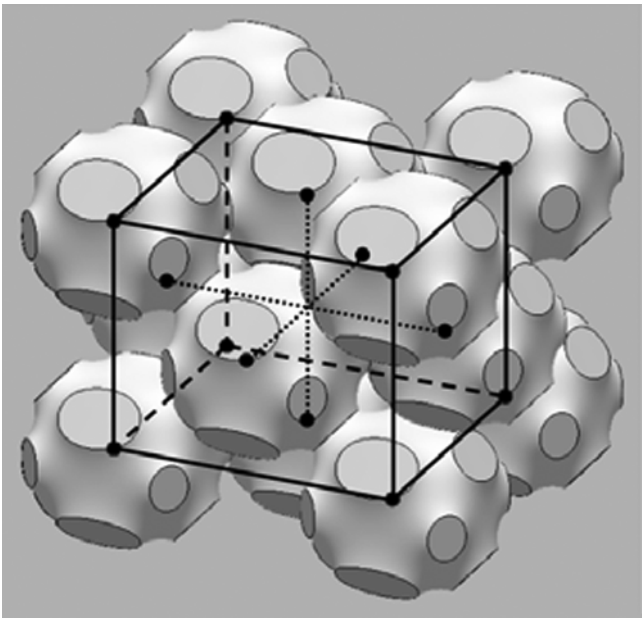

Figure 1.15. A representative volume element for sintering studies. The particle contacts are realistically represented in three dimensions with the possibility of anisotropic contacts. Reprinted with permission from Wakai and Shinoda [71], copyright 2009, Elsevier.

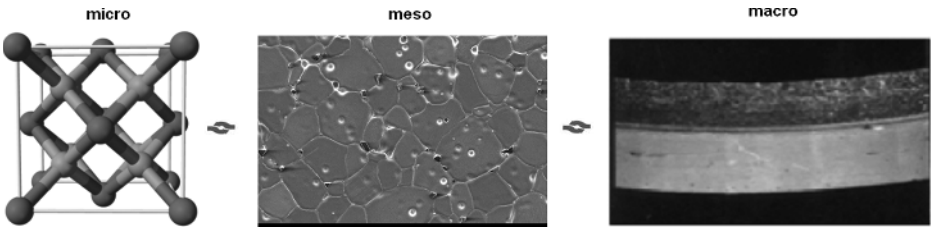

Figure 1.16. Schematic representation of the three relevant scales for sintering.

1.8 STRESS-ASSISTED SINTERING

For several crystalline materials, a high level of densification cannot be achieved by pressureless sintering. This is particularly true for covalent solids like nitrides and carbides. In these cases, external compressive stresses are used to assist the densification process. In other cases, external stresses are applied to obtain sintering in a short time and to maintain a fine-grained microstructure.

Several techniques have been developed to assist sintering with applied compressive stresses:

1. *Hot Pressing.* The powder compact is confined inside a die and the stress is applied through a piston (Fig. 1.17a).

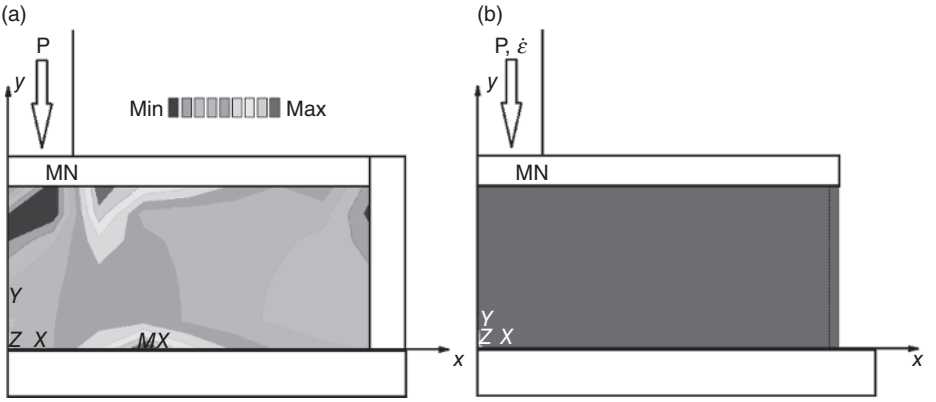

Figure 1.17. Hot pressing (a) and hot forging (b) experimental setups. The color scale represents the stress distribution. No friction is considered between die walls and platens and the powder compact. Reprinted with permission from Camacho-Montes et al. [75], copyright 2008, John Wiley & Sons.

2. *Hot Forging.* The powder compact is placed between two platens and the stress is applied in one direction. The faces of the sample that are perpendicular to the direction of the stress are free of any constraint (Fig. 1.17b).
3. *Hot Isostatic Pressing.* A powder compact is placed inside an isolated membrane and the body is subjected to hydrostatic compressive stresses (using high-pressure gas). Specialized pieces of equipment are available for these techniques. As discussed in Section 1.10, hot pressing and hot isostatic pressing are used for many important commercial ceramics.

Figure 1.17 shows the stress distribution during stress-assisted sintering assuming no friction between mold walls, the platens, and the powder compact [75]. The reason compressive stresses assist sintering is because external compressive stress acts as an additional driving force for matter transport (in addition to the surface curvature-driven local stress). Equation 1.32 shows that matter flux can increase because of stress gradients. Equations 1.24–1.26 also show that strain rate can increase because of the applied stress, which leads to an increased densification rate (Eq. 1.27). Thus, the application of external compressive stress reduces the required time for densification. This has the added advantage of reducing grain growth, leading to a more homogeneous fine-grained microstructure. In many cases, this is the primary reason for stress-assisted sintering. Hot forging has the possibility of a uniform stress distribution (Fig. 1.17b), which may be an advantage when a homogeneous structure is desired. As has been noted earlier, for most ceramics, the dependence of the densification rate on applied stress is linear (Eqs. 1.24–27) especially at low applied stresses.

The effect of applied stress on the structure evolution is an important issue to address during stress-assisted sintering. According to Equation 1.32, if the applied stresses are anisotropic, the enhancement in the flux of matter will also be anisotropic.

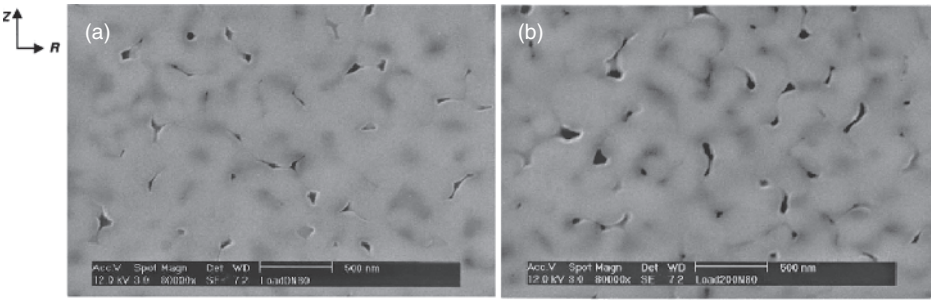

Figure 1.18. Microstructural images of alumina samples with a final density of 80% attained by (a) free sintering and (b) sinter forging, respectively, at 1250°C. Reprinted with permission from Zuo et al. [76], copyright 2003, John Wiley & Sons.

This leads to the appearance of a preferred orientation in the microstructure as can be observed in Figure 1.18 [76]. In Figure 1.18a, it can be observed that the orientation of the porosity is random during free sintering. However, during sinter forging, an anisotropic pore orientation develops with the pores oriented preferentially parallel to the applied compressive stress (Fig. 1.18b). Since in many of the stress-assisted sintering situations the microstructure becomes anisotropic, the continuum mechanics approach discussed in Section 1.6 has been modified [77].

1.9 FIELD-ASSISTED SINTERING (FAST)

In recent years, there has been significant fundamental and applied research conducted on the effect of electric fields on sintering [78–81]. The primary focus has been on the use of microwaves or a technique referred to as "spark plasma sintering" (SPS). Several advantages of the external field have been highlighted including the ability to densify in a short time, to maintain an ultrafine grain size (even nanostructured in some cases), and to densify materials without conventional sintering additives [82, 83].

Fundamentally, the effect of the field on sintering is essentially focused on the effect of the field on the mass transport. Chemical potential may be written as

$$\mu = \mu_0 + Z^* e\phi. \tag{1.38}$$

where Z^* is the valence of the diffusing ion and e is the electric charge of an electron. Hence, from Equation 1.28 and considering that the electric field E is the gradient of the electric potential ϕ, it can be stated that

$$j_{EM} = -\frac{ND}{kT} eZ^* E, \tag{1.39}$$

where j_{EM} is the flux contribution from electromigration, which is supposed to play a key role in field-assisted sintering. The activation energy for diffusion may also be affected by an applied field:

$$D = D_0 \exp\left(-\frac{U-\alpha}{kT}\right), \tag{1.40}$$

where α is the decrease in the activation energy due to the electric field. A more complex physical picture may occur in some systems when specific diffusions mechanisms may be activated because of the application of an electric field or a pulsed current.

1.9.1 SPS

Since 1933, the use of applied currents during sintering to aid in the sintering of powders or the sinter joining of metals has been reported [84]. In the 1950s, this technique was called "spark sintering." Starting in the 1960s, it has been shown that the rapidly changing electric field could also assist in the sintering of nonconducting materials (ceramics). The term "spark plasma sintering" (SPS) started in the 1960s and 1970s in Japan when it was postulated that this was due to the formation of plasma (gas of ionized particles) inside the powder compact. Since then, this field has expanded rapidly with commercial systems available for sintering materials under rapidly varying electric fields (and a modest pressure). There is very little evidence of a spark or plasma under these conditions, but the term SPS is commonly used. A more appropriate term, in our opinion, is FAST.

An important point to note is that during SPS or FAST, the temperature and current are not independent parameters, and the thermal effect of the current, that is, Joule heating, must be considered as part of the heat source. As a result, the electrical properties of the system (including the sample) are important.

FAST has been shown to offer several advantages over conventional methods including pressureless sintering and stress-assisted sintering. These advantages include lower sintering temperature, shorter holding time, and higher heating rate. Consequently, better control over the microstructure becomes a real possibility. Grain growth may be reduced drastically, and it is possible to sinter nanometric powders to near theoretical values and to maintain fine grain size. In fact, FAST is a powerful method to reach full density with negligible grain growth. Such a finer microstructural control leads to better control for the final properties and, in many cases, materials with significantly better properties. A schematic of the FAST setup is shown in Figure 1.19.

In most FAST studies, an external compressive stress is also applied. Hence, the most important parameters to control during FAST are (1) temperature, (2) electrical parameters (voltage, frequency, and power), and (3) applied pressure. Figure 1.20 illustrates the microstructure difference between samples sintered under a field and compressive stress and those sintered under only a compressive stress. The exact reasons for this difference are still under debate, but one clear advantage of FAST is the extremely rapid heating rate.

Due to its practical advantages and open scientific questions, this is an area of intense current research.

Several significant and important fundamental investigations are being conducted to understand the role of the different factors in FAST. An example is shown in

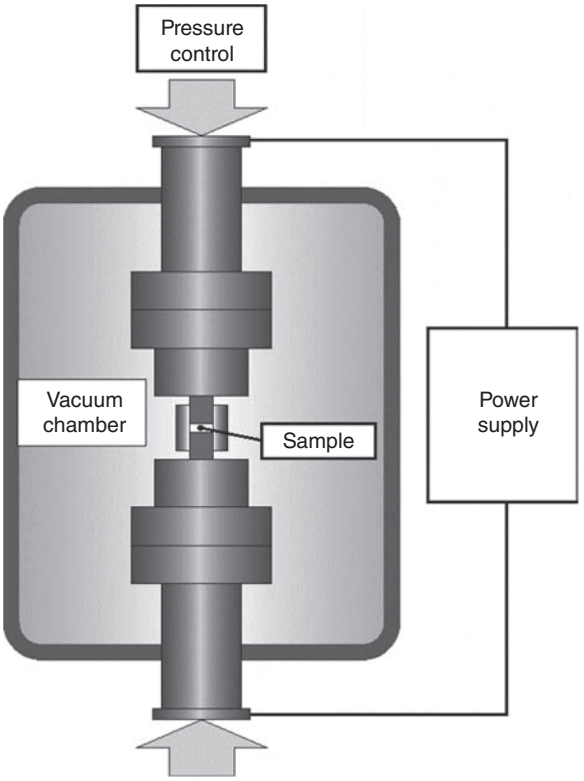

Figure 1.19. Experimental setup for field-assisted sintering (also called spark plasma sintering). Reprinted with permission from Munir et al. [82], copyright 2006, Springer.

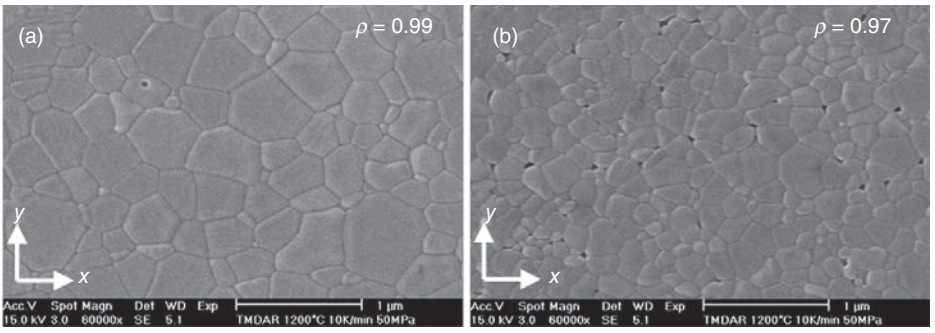

Figure 1.20. Difference between FAST and hot-pressed (HP) sintered alumina: (a) FAST and (b) HP sintered alumina at 1200°C, with a stress of 50 MPa, a heating rate of 10 K/min and a dwell time of 1 h. Reprinted with permission from Langer et al. [83], copyright 2009, Elsevier.

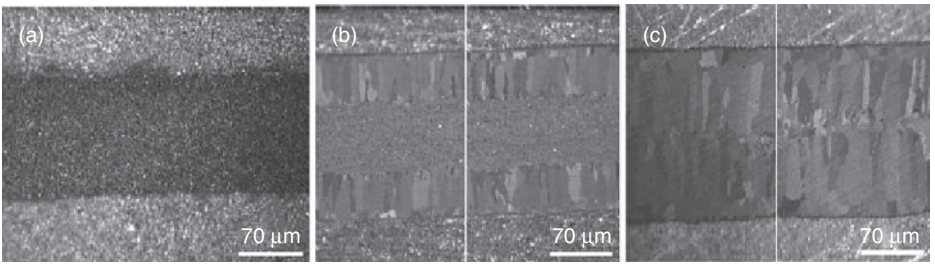

Figure 1.21. Effect of the electric current on the microstructure of an intermetallic product layer at two Al/Au interfaces, annealed at 450°C for 4 h (outer layers are Al and inside layer is Au): (a) no current, (b) current density = 0.51×10^3 A/cm^2, and (c) current density = 1.02×10^3 A/cm^2. Reprinted with permission from Munir et al. [82], copyright 2006, Springer.

Figure 1.21, where the focus is on the effect of the electric current on the microstructure. This result suggests that the applied current regime may offer a powerful technique for microstructural control. As a general rule, FAST is used to reach high densification, but, regarding microstructural control, the optimum electric field conditions may be determined by the material composition.

1.9.2 Microwave-Assisted Sintering

The use of microwaves in ceramic processing is a relatively recent development. Microwave heating is a volumetric phenomena involving conversion of electromagnetic waves (energy) into thermal energy across the entire volume. It works only with nonconducting ceramics and only with those that couple to the microwaves. In recent years, it has been successfully used to sinter a broad range of ceramics and specific advantages have been demonstrated [85–91].

Although additional research is necessary to fully understand the sintering mechanism involved in microwave-assisted sintering, the important features have been identified. First, microwave heating may be characterized by the transformation of electromagnetic energy into thermal energy. Electromagnetic dissipation may be described as

$$P = 2\pi f \varepsilon_0 \varepsilon_r' \tan\delta |E|^2, \tag{1.41}$$

where f, ε_0, and ε_r' are the electric field lineal frequency, the vacuum dielectric conductivity, and the sintering material relative dielectric constant. $\tan\delta$ is the loss tangent and is given by

$$\tan\delta = \frac{\varepsilon''}{\varepsilon'} = \frac{\varepsilon_r''}{\varepsilon_r'}, \tag{1.42}$$

where ε'' and ε' are known as the imaginary and real parts of the complex dielectric constant. The subscript r is referred relative to the vacuum dielectric constant. The

imaginary part describes the ability of the material to dissipate the electric field energy into heat. However, the loss tangent is easier to directly measure it.

Hence, the loss factor characterizes the ability of the material to transform the microwave energy into heat. The heating due to the absorbed microwaves inside of the powder compact leads to an increase in its temperature given by

$$\frac{\Delta T}{\Delta t} = \frac{2\pi f \varepsilon_0 \varepsilon_r'' |E|^2}{\rho C_p}. \tag{1.43}$$

ρ and C_p are the apparent density and the heat capacity per unit mass. The depth of penetration is also an important parameter to be considered for the experimental setup since it determines the uniformity of heating, that is, the uniformity of the energy supply for any sintering-related phenomena such as densification and grain growth. High frequency and large values of the dielectric property will result in only near surface heating, which may lead to nonuniform microstructure and stress gradients between the bulk and the surface due to the different densification rate. Low frequencies and small values of dielectric properties will result in a more volumetric heating with higher possibilities of uniform microstructure and densification. It can be expressed as

$$d = \frac{3\lambda_0}{8.686\pi f \tan\delta \sqrt{\varepsilon_r' / \varepsilon_0}}, \tag{1.44}$$

where λ_0 is the microwave incident wave length.

The microwave part of the electromagnetic spectrum corresponds to frequencies between 300 MHz and 300 GHz. In general, the higher the frequency, the higher is the power dissipation (Eq. 1.41). Because of this and for practical reasons (equipment design), most sintering applications of microwaves are in the range of 915 MHz–2.45 GHz. Based on their microwave interaction, most materials can be classified into one of three categories—opaque, transparent, and absorbers. For microwaves to effectively heat the material, it must be a good absorber of microwaves. For ceramics, the degree of microwave absorption (Eq. 1.44), and consequently the heating rate (Eq. 1.43), strongly depends on ε polarization and loss factor $\tan\delta$.

The most significant advantage of microwave heating is that it is a volumetric effect. The microwave heating is from the core of the sample to the surface (Fig. 1.22b).

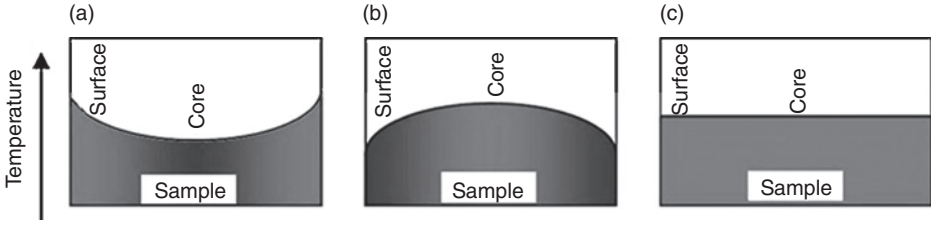

Figure 1.22. Temperature profile within the sample in (a) conventional heating, (b) microwave heating, and (c) microwave hybrid heating. Reprinted with permission from Oghbaei and Mirzaee [92], copyright 2010, Elsevier.

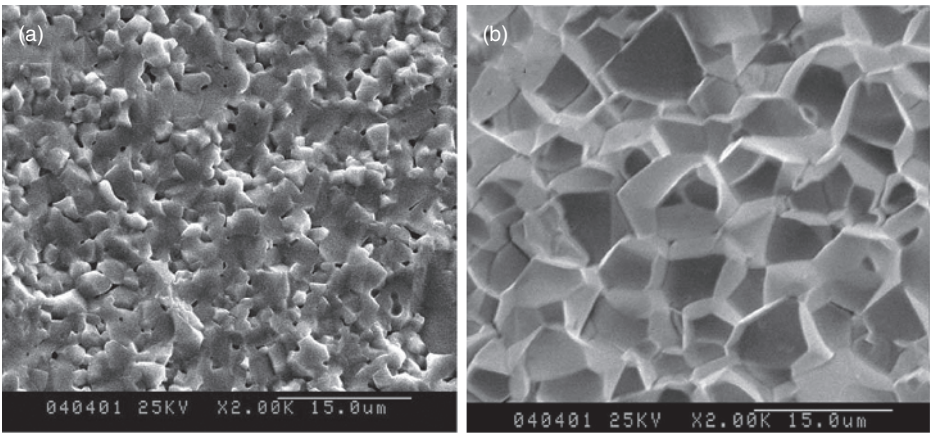

Figure 1.23. Scanning electron microscopy (SEM) micrographs of Ni–Zn–Cu ferrite samples sintered at 980°C by the (a) conventional sintering technique and the (b) microwave sintering technique. Reprinted with permission from Oghbaei and Mirzaee [92], copyright 2010, Elsevier.

In conventional heating, on the other hand, the surface is heated by convection and then the interior by conduction through the sample (Fig. 1.22a). Since most ceramics are poor conductors of heat, the temperature gradients, especially in conventional heating, can be significant. Thus, both microwave and conventional heating can lead to temperature nonuniformities and possible inhomogeneous densification. One solution is to combine the two heating methods. This method is known as microwave hybrid heating, and the possible temperature distribution with this approach is schematically shown in Figure 1.22c.

In fact, the reaction between microwaves and materials also leads to a change in the microstructural evolution as may be described by Equations 1.39 and 1.40. A much faster heating rate (Eq. 1.43) may induce a more homogeneous microstructure with less grain growth. One of the main advantages of microwave hybrid heating is the uniformity of the microstructure. Figure 1.23 shows the difference between the microstructure of Ni–Zn–Cu ferrites sintered under conventional and microwave heating.

The processing advantages of microwave heating over conventional ones may be summarized as rapid heating rates and considerable reduction in sintering time and temperature. Generally, a higher density and a more uniform grain size distribution can be achieved through microwave sintering. In addition, microwave sintering is an attractive approach to sinter samples of large sizes.

1.10 SINTERING PRACTICE

The developments in sintering theory summarized above have, at least, led to a qualitative description of the effect of critical parameters on densification and final microstructure.

It has been recognized that the control of the green compact is particularly important in sintering practice [93]. To achieve a dense fine-grained sintered body, it is desirable to have small particles with a narrow size distribution. The powder should be nonagglomerated, equiaxed, and of high purity or controlled dopant level [94]. These requirements have led to the development of chemical techniques to produce ceramic powders of high purity and controlled size. In addition, emphasis has been placed on green state processing, in particular, ways to avoid agglomeration by pH and counterion control in aqueous systems [95], or stabilization of the colloids by surfactants [96].

Using sintering science as a guide, Yan identified the desired conditions during sintering to obtain good microstructural control during densification [9]. In addition to the desired characteristics of the green compact highlighted above, the other important factors are dopant level, sintering atmosphere, and firing schedule. Although each of these has to be optimized for a specific system, some general guidelines are clear. Basically, the nondensifying (i.e., the coarsening) mechanisms should be suppressed and the densifying mechanisms should be promoted. Therefore, dopants, sintering atmosphere, and heating schedules that favor grain boundary and/or volume diffusion over surface diffusion and vapor transport are desirable. In addition, conditions that minimize exaggerated grain growth (so that pores are not trapped in the grain in the final stages) are favored. Several strategies have been devised to ensure this, including the use of appropriate dopants [9] or by making use of the second phase (in some cases transient) to pin grain boundaries [97].

A classic and technologically important example of the role of dopants is the use of MgO as a dopant in Al_2O_3 [98]. It is now well-known that MgO-doped Al_2O_3 does not undergo abnormal grain growth and hence can be sintered to high density. Since then, the mechanism of this effect has been a topic of significant research and controversy [99, 100]. There is agreement that MgO reduces the grain growth rate. However, the mechanism for this continues to be debated.

An example of the effect of sintering atmosphere is that Al_2O_3 doped with MgO can be sintered to full density (translucent) in a hydrogen or oxygen environment but not in air, nitrogen, argon, or helium [101]. This is because hydrogen and oxygen have good solubility and high diffusivity in Al_2O_3. Another important feature that has been recognized is the interaction between dopants and the atmosphere. Usually, these reactions have the tendency to remove the dopants and thereby reduce their effectiveness. Therefore, in general, these reactions should be avoided.

Finally, the heating schedule has been shown to have a significant effect on densification and final microstructure. This is because in general, the rate-controlling transport mechanism for densification, grain growth, and coarsening has different activation energies and hence dominates in different temperature regimes. In general, the coarsening mechanisms dominate at lower temperatures (due to lower activation energies). Three significant developments are noteworthy. In rate-controlled sintering, the heating rate is controlled to maintain a constant densification rate. It has been shown that this type of heating profile minimizes grain growth [102]. In fast firing, the temperature is raised rapidly and held at a high temperature for a short time. This minimizes the time spent in temperature regions in which the coarsening mechanisms dominate [103]. Finally, FAST (discussed in Section 1.9) may be an example of the effectiveness of controlling the heating rate.

1.10.1 Processing Defects

A major concern in sintering is the effect of the green structure and processing parameters on the defects in the sintered microstructure. These processing flaws have been postulated to be the main cause of the poor reliability of structural ceramics [104]. A very thorough and comprehensive study that clearly highlights the effect of processing on strength-limiting defects was conducted by Lange and coworkers. The material chosen for this study was 0.7 Al_2O_3–0.3 ZrO_2. First, these materials were dry pressed and sintered. The average flexural strength was found to be 560 MPa. From fractography, the strength-limiting flaws were found to be soft agglomerates, which sintered away from the matrix, leaving behind large circumferential cracks [105]. These soft agglomerates were removed by using colloidal processing followed by slip casting and sintering. These materials had an average flexure strength of 895 MPa. The strength-limiting flaws in these materials were small hard agglomerates [106, 107]. Finally, in the next step, these agglomerates were removed by sedimentation prior to slip casting. These materials had an average flexure strength of 1045 MPa, in which the strength-limiting flaws were irregularly shaped cracks postulated to be the burnout of organic inclusions (e.g., lint).

It has been shown that differential densification rates in inhomogeneous powder compacts lead to internal stresses during sintering [108]. For an inclusion with a sintering rate less than the matrix, the circumferential stress at the interface between the inclusion and the matrix is tensile. This could lead to radial cracks. On the other hand, for an inclusion that sinters faster than the matrix, the radial stresses are tensile, which can lead to circumferential cracks. In Reference 109, it has been shown that there is a critical inclusion (or inhomogeneity size) such that for inclusions less than this, cracks are not formed. The critical size depends on the difference in the sintering rate and the constitutive parameters (particularly the viscous Poisson's ratio).

1.11 SUMMARY

Sintering is an important approach to manufacture ceramics and hard metals of controlled density. It is used for a broad range of applications, from pottery to high-tech electronic and structural ceramics. In the last 70 years, our understanding of sintering science and technology has advanced considerably.

This chapter provides an overview of these advances. The basics, including the thermodynamics and kinetics of sintering, have been presented. The various models for sintering of powder compacts in different geometric stages have been discussed for different types of sintering (viscous, solid state, and liquid phase). Some of the important areas of current research including the sintering of multicomponent materials (constrained sintering), microstructure-based models, multiscale models, sintering under external stresses, and FAST are summarized. The important lessons from the science and their application in sintering practice have also been highlighted.

Although considerable progress has been made, several areas of active research remain. In addition to the emerging areas like constrained sintering and FAST, the

precise, quantitative description of sintering remains an active area of research and development. The microstructure-based models and multiscale modeling are promising approaches.

ACKNOWLEDGMENT

RKB acknowledges partial support during the writing of this chapter from the Air Force Office of Scientific Research (FA95550-09-1-0633) and from the National Science Foundation (DMR-1008600). RKB and HCM gratefully acknowledge the support of Consejo Nacional de Ciencia y Tecnología (Mexico) for the sabbatical stay of HCM in the research group of RKB.

REFERENCES

1. S. L. Sass, *The Substance of Civilization: Materials and Human History from the Stone Age to the Age of Silicon*. Arcade Publishing, New York, 1998.
2. R. F. Walker (1955) Mechanism of materials transport during sintering, *J. Am. Ceram. Soc.*, **38** 187–197.
3. H. H. Hausner, *Handbook of Powder Metallurgy*, Chemical Publishing, New York, 1973.
4. F. J. Klug, W. D. Pasco, and M. P. Borom (1982) Microstructure development of aluminum oxide: Graphite mixure during carbothermic reduction, *J. Am. Ceram. Soc.*, **65** 619–624.
5. F. Thümmler and W. Thomma (1967) The sintering process, *Metall. Rev.*, **12** 69–108.
6. W. J. Huppman, in *Sintering and Catalysis*, ed. G. C. Kuczynski, p. 359, Plenum Press, New York, 1975.
7. H. E. Exner and G. Petzow, in *Sintering Process*, ed. G. C. Kuczynski, p. 107, Plenum Press, New York, 1980.
8. R. L. Coble and R. M. Cannon, in *Processing of Crystalline Solids*, eds. H. Palmour, III, R. F. Davis, and T. M. Hare, p. 151, Plenum Press, New York, 1978.
9. M. F. Yan (1981) Microstructural control in the processing of electronic ceramics, *Mat. Sci. Eng.*, **48** 53–72.
10. H. E. Exner and E. Arzt, in *Physical Metallurgy*, 3rd edition, Chapter 30, eds. R. W. Cahn and P. Hassen, pp. 1885–1912, Elsevier Science Publishers, Amsterdam, 1983.
11. C. A. Handwerker, J. E. Blendell, and W. A. Kaysser (eds.), in *Sintering of Advanced Ceramics: Ceramics Transactions*, Vol. 7, The American Ceramic Society, Westerville, OH, 1989.
12. R. M. German, *Sintering Theory and Practice*, John Wiley & Sons, New York, 1996.
13. R. M. German, G. L. Messing, and R. G. Cornwall (eds.), *Sintering Technology*, Marcel Dekker, New York, 1996.
14. S.-J. L. Kang, *Sintering Densification, Grain Growth and Microstructure*. Elsevier Butterworth-Heinemann, Burlington, VT, USA, 2005.
15. R. Bordia and E. Olevsky (2009) Guest Editors for Advances in sintering science and technology, special issue of the *J. Am. Ceram. Soc.*, **92**[7] 1383.
16. R. K. Bordia and E. Olevsky (eds.), *Advances in Sintering Science and Technology: Ceramic Transactions*, Vol. 209, The American Ceramic Society, Westerville, OH, 2010.

17. R. L. Coble (1961) Sintering crystalline solids. intermediate and final state diffusions models, *J. Appl. Phys.*, **32** 787–792.
18. J. I. Martínez-Herrera and J. J. Derby (1995) Viscous sintering of spherical particles via finite element analysis, *J. Am. Ceram. Soc.*, **78**[3] 645–649.
19. J. Frenkel (1945) Viscous flow of crystalline bodies under the action of surface tension, *J. Phys. USSR*, **9** 385–391.
20. G. W. Scherer (1991) Cell models for viscous sintering, *J. Am. Ceram. Soc.*, **74**[7] 1523–1531.
21. J. K. Mackenzie and R. Shuttleworth (1949) A phenomenological theory of sintering, *Proc. Phys. Soc. B*, **62**[12] 833–852.
22. W. D. Kingery, H. K. Bowen, and D. R. Uhlmann, *Introduction to Ceramics*, A Wiley-Interscience Publication, John Wiley & Sons, New York, 1975.
23. G. C. Kuczynski (1949) Self-diffusion in sintering of metallic particles, *Trans. AIME*, **185** 169–178.
24. M. F. Ashby (1974) A first report on sintering diagrams, *Acta Metall.*, **22** 275–289.
25. F. B. Swinkles and M. F. Ashby (1981) A second report on sintering diagrams, *Acta Metall.*, **29** 259–281.
26. C. Herring (1950) Effect of change of scale on sintering phenomena, *J. Appl. Phys.*, **21** 301–303.
27. W. K. Burton, N. Cabrera, and F. C. Frank (1951) The growth of crystals and the equilibrium structure of their surfaces, *Philos. Trans. R. Soc.*, **243A** 299–358.
28. Y. E. Geguzin, L. O. Markno, and B. Y. Pines (1952) Self-diffusion and viscous flow (sintering and creep) in compressed metal powders, *Dokl. Akad. Nauk SSSR*, **87**[4] 577–580.
29. J. G. R. Rockland (1966) On the rate equation for sintering by surface diffusion, *Acta Metall.*, **14** 1273–1279.
30. J. G. R. Rockland (1967) The determination of the mechanism of sintering, *Acta Metall.*, **15** 277–286.
31. W. D. Kingery and M. Berg (1955) Study of the initial stages of sintering solids by viscous flow, evaporation-condensation, and self-diffusion, *J. Appl. Phys.*, **26** 1205–1212.
32. P. V. Hobbs and B. J. Mason (1964) The sintering and adhesion of ice, *Phil. Mag.*, **9** 181–197.
33. R. L. Coble (1958) Initial sintering of alumina and hematite, *J. Am. Ceram. Soc.*, **41** 55–62.
34. D. L. Johnson (1969) New method of obtaining volume, grain-boundary, and surface diffusion coefficients from sintering data, *J. Appl. Phys.*, **40** 192–200.
35. D. L. Johnson (1970) A general model for the intermediate stage of sintering, *J. Am. Ceram. Soc.*, **53** 574–577.
36. R. L. Eadie and G. C. Weatherly (1975) Solutions for the shrinkage rate in the intermediate stage of sintering, *Scr. Metall.*, **9** 285–294.
37. R. L. Eadie, G. C. Weatherly, and K. T. Aust (1978) A study of sintering of spherical silver powder—I. The intermediate stage, *Acta Metall.*, **26** 759–767.
38. W. K. Beere (1975) A unifying theory of the stability of penetrating liquid phases and sintering pores, *Acta Metall.*, **23** 131–138.
39. W. K. Lee, R. L. Eadie, G. C. Weatherly, and K. T. Aust (1976) Method for three-dimensional studies of sintering compacts, *Prakt. Metall./Pract. Metall.*, **13**[5] 241–247.

40. W. Beere, in *Vacancies'76*, eds. R. E. Smallman and J. E. Harris, p. 149, The Metals Society, London, 1977.
41. G. C. Kuczynski (1977) Science of sintering, *Sci. Sinter.*, **9**[3] 243–264.
42. R. Raj and M. F. Ashby (1975) Intergranular fracture at elevated temperature, *Acta Metall.*, **23** 653–666.
43. D. Hull and D. E. Rimmer (1959) The growth of grain-boundary voids under stress, *Phil. Mag.*, **4**[42] 673–687.
44. R. Raj, H. M. Shih, and H. H. Johnson (1977) Correction to: Intergranular fracture at elevated temperature, *Scr. Metall.*, **11** 839–842.
45. B. H. Alexander and R. W. Balluffi (1957) The mechanism of sintering of copper, *Acta Metall.*, **5** 666–677.
46. J. E. Burke, in *Ceramic Microstructures*, eds. R. M. Fulrath and J. A. Pask, p. 681, Wiley, New York, 1968.
47. K. W. Lay, in *Sintering and Related Phenomenon*, eds. G. C. Kuczynski, p. 65, Plenum Press, New York, 1973.
48. W. D. Kingery and B. Francois, in *Sintering and Related Phenomenon*, eds. G. C. Kuczynski, N. A. Hooten, and C. F. Gibbon, p. 471, Gordon Breach, New York, 1967.
49. R. J. Brook (1969) Pore-grain boundary interactions and grain growth, *J. Am. Ceram. Soc.*, **52** 56–57.
50. C. H. Hsueh, A. G. Evans, and R. L. Coble (1982) Microstructure development during final/intermediate stage sintering—I. Pore/grain boundary separation, *Acta Metall.*, **30** 1269–1279.
51. M. Sakarcan, C. H. Hsueh, and A. G. Evans (1983) Experimental assessment of pore breakaway during sintering, *J. Am. Ceram. Soc.*, **66** 456–461.
52. B. J. Kellett and F. F. Lange (1989) Thermodynamics of densification. I. Sintering of simple particle arrays, equilibrium configurations, pore stability, and shrinkage, *J. Am. Ceram. Soc.*, **71**[5] 725–734.
53. R. M. German, P. Suri, and S. J. Park (2009) Review: Liquid phase sintering, *J. Mater. Sci.*, **44** 1–39.
54. M. N. Rahaman, *Ceramic Processing and Sintering*, 2nd edition, CRC Press, New York, 2003.
55. R. M. German, *Liquid Phase Sintering*, 1st edition, Plenum Press, New York, 1985.
56. R. K. Bordia and G. W. Scherer (1988) On constrained sintering—I. Constitutive model for a sintering body, *Acta Metall.*, **36**[9] 2393–2417.
57. R. K. Bordia and G. W. Scherer (1988) On constrained sintering—II. Comparison of constitutive models, *Acta Metall.*, **36**[9] 2393–2417.
58. E. A. Olevsky (1998) Theory of sintering from discrete to continuum, *Mater. Sci. Eng.*, **R23**[2] 41–100.
59. R. K. Bordia and G. W. Scherer (1988) Constrained sintering: III. Rigid inclusions, *Acta Metall.*, **36** 2411–2416.
60. S. M. Salamone, L. C. Stearns, R. K. Bordia, and M. P. Harmer (2003) Effect of rigid inclusions on the densification and constitutive parameters of liquid phase sintered $YBa_2Cu_3O_{6+x}$ powder compacts, *J. Am. Ceram. Soc.*, **86**[6] 883–892.
61. R. K. Bordia and R. Raj (1985) Sintering behavior of ceramic films constrained by a rigid substrate, *J. Am. Ceram. Soc.*, **68**[6] 287–292.

62. R. K. Bordia and A. Jagota (1993) Crack growth and damage in constrained sintering films, *J. Am. Ceram. Soc.*, **76**[10] 2475–2485.
63. O. Guillon, E. Aubach, R. K. Bordia, and J. Rödel (2007) Constrained sintering of alumina thin films: Comparison between experiments and modeling, *J. Am. Ceram. Soc.*, **90**[6] 1733–1737.
64. J. Svoboda, H. Riedel, and H. Zipse (1994) Equilibrium pore surfaces, sintering stresses and constitutive equations for the intermediate and late stage of sintering—I. Computation of equilibrium surfaces, *Acta Metall. Mater.*, **42**[2] 435–443.
65. H. Riedel, H. Zipse, and J. Svoboda (1994) Equilibrium pore surfaces, sintering stresses and constitutive equations for the intermediate and late stage of sintering—II. Diffusional densification and creep, *Acta Metall. Mater.*, **42**[2] 445–452.
66. T. Kraft and H. Riedel (2004) Numerical simulation of solid state sintering; model and application, *J. Eur. Ceram. Soc.*, **24** 345–361.
67. C. L. Martin, L. C. R. Schneider, L. Olmos, and D. Bouvard (2006) Discrete element modeling of metallic powder sintering, *Scr. Mater.*, **55** 425–428.
68. A. Wonisch, O. Guillon, T. Kraft, M. Moseler, H. Riedel, and J. Rodel (2007) Stress-induced anisotropy of sintering alumina: Discrete element modelling and experiments, *Acta Mater.*, **55** 5187–5199.
69. C. L. Martin and R. K. Bordia (2009) The effect of substrate on the sintering of constrained films, *Acta Mater.*, **57**[2] 549–558.
70. C. L. Martin, H. Camacho-Montes, L. Olmos, D. Bouvard, and R. K. Bordia (2009) Evolution of defects during sintering: Discrete element simulations, *J. Am. Ceram. Soc.*, **92**[7] 1435–1441.
71. F. Wakai and Y. Shinoda (2009) Anisotropic sintering stress for sintering of particles arranged in orthotropic symmetry, *Acta Mater.*, **57** 3955–3964.
72. D. J. Green, O. Guillon, and J. Rödel (2008) Constrained sintering: A delicated balance of scales, *J. Eur. Ceram. Soc.*, **28** 1451–1466.
73. E. A. Olevsky, V. Tikare, and T. Garino (2006) Multi-scale study of sintering: A review, *J. Am. Ceram. Soc.*, **89**[6] 1914–1922.
74. A. Kuzmov, E. Olevsky, and A. Maximenko (2008) Multi-scale modeling of viscous sintering, *Modell. Simul. Mater. Sci. Eng.*, **16** 035002 10 pp.
75. H. Camacho-Montes, P. E. García-Casillas, R. Rodríguez-Ramos, M. E. Fuentes-Montero, and L. E. Fuentes-Cobas (2008) Simulation of stress-assisted densification behavior of a powder compact: Effect of constitutive laws, *J. Am. Ceram. Soc.*, **91** 836–845.
76. R. Zuo, E. Aulbach, R. K. Bordia, and J. Rodel (2003) Critical evaluation of hot forging experiments: Case study in alumina, *J. Am. Ceram. Soc.*, **86**[7] 1099–1105.
77. R. K. Bordia, R. Zuo, O. Guillon, S. M. Salamone, and J. Rödel (2006) Anisotropic constitutive laws for sintering bodies, *Acta Mater.*, **54** 111–118.
78. G. Bernard-Granger and C. Guizard (2007) Spark plasma sintering of a commercially available granulated zirconia powder: I. Sintering path and hypotheses about the mechanism(s) controlling densification, *Acta Mater.*, **55** 3493–3504.
79. Z. Shen, M. Johnsson, Z. Zhao, and M. Nygren (2002) Spark plasma sintering of alumina, *J. Am. Ceram. Soc.*, **85**[8] 1921–1927.
80. J. Räthel, M. Herrmann, and W. Beckert (2009) Temperature distribution for electrically conductive and non-conductive materials during field assisted sintering (FAST), *J. Eur. Ceram. Soc.*, **29** 1419–1425.

81. Y. Zhou, K. Hirao, Y. Yamauchi, and S. Kanzaki (2004) Densification and grain growth in pulse electric current sintering of alumina, *J. Eur. Ceram. Soc.*, **24** 3465–3470.
82. Z. A. Munir, U. Anselmi-Tamburini, and M. Ohyanagi (2006) The effect of electric field and pressure on the synthesis and consolidation of materials: A review of the spark plasma sintered method, *J. Matter Sci.*, **41** 763–777.
83. J. Langer, M. J. Hoffmann, and O. Guillon (2009) Direct comparison between hot pressing and electric field-assisted sintering of submicron alumina, *Acta Mater.*, **57** 5454–5465.
84. G. F. Taylor (1933) U.S. Patent No. 1,896,854.
85. S. Nath, B. Basu, and A. Sinha (2006) A comparative study of conventional sintering with microwave sintering of hydroxyapatite synthesized by chemical route, *Trends Biomater. Artif. Organs*, **19**[2] 93–98.
86. A. Chatterjee, T. Basak, and K. G. Ayappa (1998) Analysis of microwave sintering of ceramics, *Materials, Interfaces, and Electrochemical Phenomena. AIChE J.*, **44**[10] 2302–2311.
87. K. E. Haque (1999) Microwave energy for mineral treatment processes—A brief review, *Int. J. Miner. Process.*, **57** 1–24.
88. D. E. Clark (1996) Microwave processing of materials, *Annu. Rev. Mater. Sci.*, **26** 299–331.
89. E. T. Thostenson and T.-W. Chou (1999) Microwave processing: Fundamentals and applications, *Composites A*, **30** 1055–1071.
90. J. D. Katz (1992) Microwave sintering of ceramics, *Annu. Rev. Mater. Sci.*, **22** 153–170.
91. D. E. Clark, D. C. Folz, and J. K. West (2000) Processing materials with microwave energy, *Mater. Sci. Eng.*, **A287** 153–158.
92. M. Oghbaei and O. Mirzaee (2010) Microwave versus conventional sintering: A review of fundamentals, advantages and applications, *J. Alloys Comp.*, **494** 175–189.
93. G. Y. Onoda, Jr. and L. L. Hench (eds.), *Ceramic Processing before Firing*. John Wiley, New York, 1978.
94. P. Reynen, in *Sintering Proceesses* ed. G. C. Kuczynski, pp. 46–54, Plenum Press, New York, 1980.
95. P. J. Anderson and P. Murray (1959) Zeta potentials in rheological properties of oxide slips, *J. Am. Ceram. Soc.*, **42** 70–74.
96. G. D. Parfitt and J. Peacock, in *Surface and Colloid Science*, ed. E. Matijevic, p. 163, Wiley-Interscience, New York, 1978.
97. W. H. Rhodes (1981) Controlled transient solid second-phase sintering of yttria, *J. Am. Ceram. Soc.*, **64** 13–19.
98. W. C. Johnson and R. L. Coble (1978) A test of the second-phase and impurity segregation models for MgO-enhanced densification of sintered alumina, *J. Am. Ceram. Soc.*, **61**[3–4] 110–114.
99. S. J. Bennison and M. P. Harmer (1988) History of the role of MgO in the sintering of alpha-Al_2O_3, *Cer. Trans.*, **7** 13–49.
100. I.-J. Bae and S. Baik (1997) Abnormal grain growth of alumina, *J. Am. Ceram. Soc.*, **80**[5] 1149–1156.
101. R. L. Coble (1962) Sintering alumina: Effect of atmospheres, *J. Am. Ceram. Soc.*, **45** 123–127.

102. H. Palmour, III, M. L. Huckabee, and T. M. Hare Rate controlled sintering: Principles and practice. Sintering—New Developments, Fourth International Round Table Conference on Sintering, Elsevier, Amsterdam 46–56, 1979.

103. M. P. Harmer, *Rapid sintering of pure and doped alpha alumina*, PhD thesis, University of Leeds, Leeds, UK, 1980.

104. F. F. Lange (1984) Structural ceramics: A question of fabrication reliability, *J. Mat. Energy Syst.*, **6**[2] 107–113.

105. F. F. Lange (1983) Processing-related fracture origins: I, observations in sintered and isostatically hot-pressed Al_2O_3/ZrO_2 composites, *J. Am. Ceram. Soc.*, **66** 396–398.

106. I. A. Aksay, F. F. Lange, and B. A. Davis (1983) Uniformity of Al_2O_3-ZrO_2 composites by colloidal filtration, *Comm. J. Am. Ceram. Soc.*, **66** C190–C192.

107. F. F. Lange, B. A. Davis, and I. A. Aksay (1983) Processing-related fracture origins: III, differential sintering of ZrO_2 agglomerates in Al_2O_3/ZrO_2 composite, *J. Am. Ceram. Soc.*, **66** 407–408.

108. R. K. Bordia and G. W. Scherer, *Ceramic Transactions*, Vol. 1, eds. G. L. Messing, E. R. Fuller, Jr., and H. Hausner, pp. 872–886, American Ceramic Society, Westerville, OH, 1988.

109. R. Raj and R. K. Bordia (1984) Sintering behavior of bi-modal powder compacts, *Acta Metall.*, **32**[7] 1003–1019.